

Evolution of enhanced innate immune suppression by SARS-CoV-2 Omicron subvariants

Received: 22 July 2022

Accepted: 13 December 2023

Published online: 16 January 2024

 Check for updates

Ann-Kathrin Reuschl¹✉, Lucy G. Thorne^{1,2}, Matthew V. X. Whelan¹, Roberta Ragazzini^{1,3}, Wilhelm Furnon⁴, Vanessa M. Cowton⁴, Giuditta De Lorenzo⁴, Dejan Mesner¹, Jane L. E. Turner¹, Giulia Dowgier^{1,5}, Nathasha Bogoda¹, Paola Bonfanti^{1,3}, Massimo Palmarini⁴, Arvind H. Patel⁴, Clare Jolly^{1,6}✉ & Greg J. Towers^{1,6}✉

Severe acute respiratory syndrome coronavirus 2 (SARS-CoV-2) human adaptation resulted in distinct lineages with enhanced transmissibility called variants of concern (VOCs). Omicron is the first VOC to evolve distinct globally dominant subvariants. Here we compared their replication in human cell lines and primary airway cultures and measured host responses to infection. We discovered that subvariants BA.4 and BA.5 have improved their suppression of innate immunity when compared with earlier subvariants BA.1 and BA.2. Similarly, more recent subvariants (BA.2.75 and XBB lineages) also triggered reduced innate immune activation. This correlated with increased expression of viral innate antagonists Orf6 and nucleocapsid, reminiscent of VOCs Alpha to Delta. Increased Orf6 levels suppressed host innate responses to infection by decreasing IRF3 and STAT1 signalling measured by transcription factor phosphorylation and nuclear translocation. Our data suggest that convergent evolution of enhanced innate immune antagonist expression is a common pathway of human adaptation and link Omicron subvariant dominance to improved innate immune evasion.

Severe acute respiratory syndrome coronavirus 2 (SARS-CoV-2) variants of concern (VOCs) Alpha, Delta and then Omicron became sequentially dominant globally, with each evolving independently from wave 1 early lineage SARS-CoV-2 virus. Sequential lineage replacement suggests evolution of highly advantageous characteristics that effectively improved transmission. Our previous work showed that Alpha¹, and also VOCs Beta to Delta², adapted by enhancing expression of specific innate immune antagonists including Orf6, N and Orf9b, to suppress the host innate immune response initiated on infection. Since the appearance of

the Omicron lineage, it is Omicron subvariants that are co-circulating, or being replaced by each other, rather than new, wave 1-derived, VOCs. The selective forces driving SARS-CoV-2 evolution may therefore have switched from being predominantly adaptation-to-host to immune escape from vaccine- and infection-driven memory responses. In fact, the first dominant Omicron subvariants BA.1 and BA.2, BA.4 and BA.5 emerged with each displaying increasing levels of antibody escape, through mutation of spike, threatening vaccine efficacy and increasing hospitalizations^{3–16}. However, like Alpha to Delta, Omicron subvariants

¹Division of Infection and Immunity, University College London, London, UK. ²Department of Infectious Diseases, St Mary's Medical School, Imperial College London, London, UK. ³Epithelial Stem Cell Biology and Regenerative Medicine Laboratory, The Francis Crick Institute, London, UK.

⁴MRC-University of Glasgow Centre for Virus Research, Glasgow, UK. ⁵COVID Surveillance Unit, The Francis Crick Institute, London, UK. ⁶These authors contributed equally: Clare Jolly, Greg J. Towers. ✉ e-mail: a.reuschl@ucl.ac.uk; c.jolly@ucl.ac.uk; g.towers@ucl.ac.uk

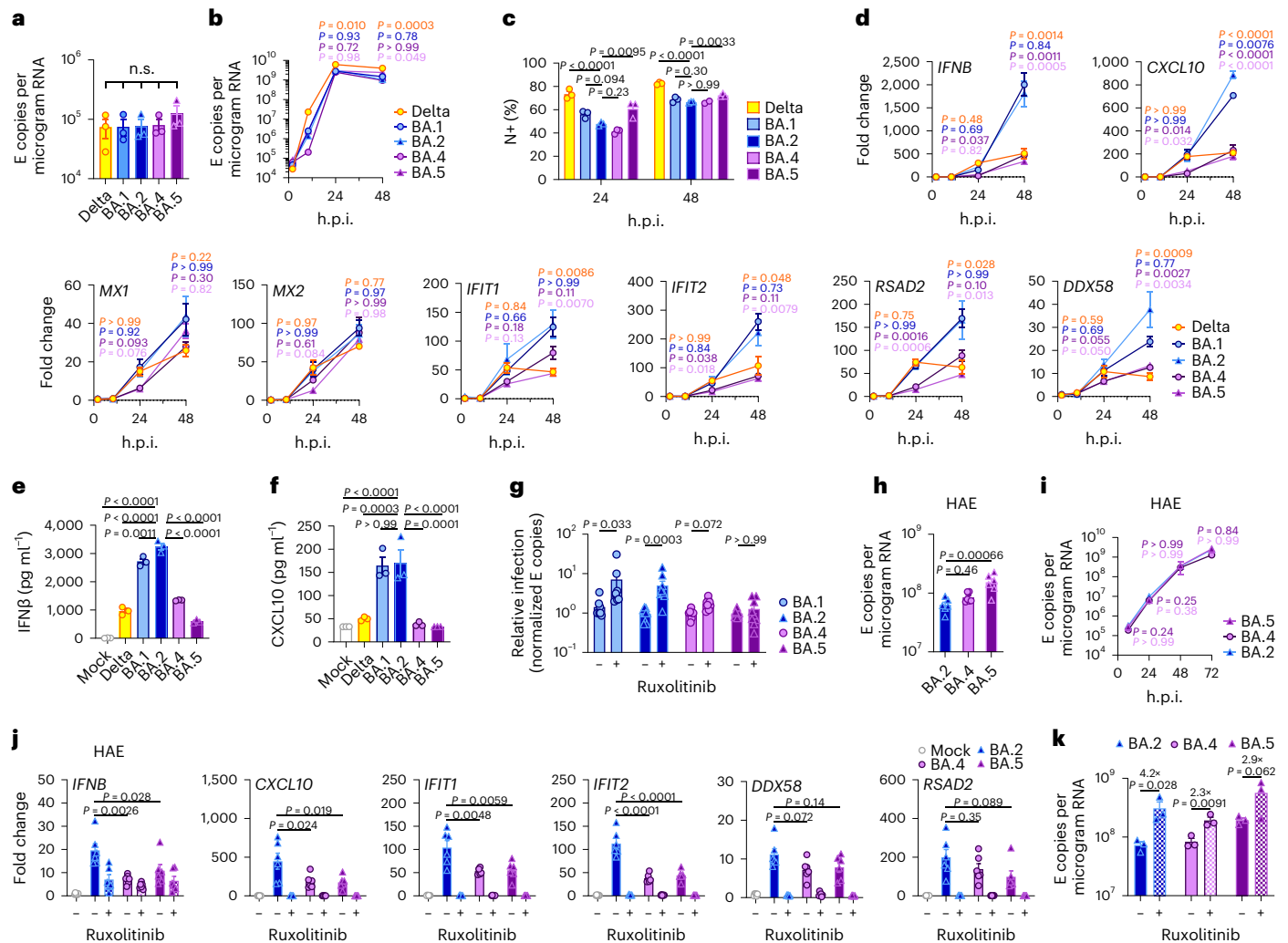


Fig. 1 | BA.5 displays enhanced innate immune antagonism during infection of airway epithelial cells. **a–g.** Calu-3 infection with 2,000 E copies per cell of Delta (yellow, O), BA.1 (blue, O), BA.2 (blue, Δ), BA.4 (purple, O) and BA.5 (purple, Δ), $n = 3$; mean viral E copies at 2 h.p.i. across three independent experiments (**a**); viral replication over time measured by RT–qPCR for intracellular E copies per microgram RNA (**b**); infection levels measured by nucleocapsid expression (% N+ by flow cytometry) (**c**); expression of *IFNB*, *CXCL10*, *IFIT1*, *IFIT2*, *RSAD2*, *MX1*, *MX2* and *DDX58* in infected cells over time (**d**); *IFNβ* (**e**) and *CXCL10* (**f**) secretion from infected Calu-3 cells measured by ELISA at 48 h.p.i.; rescue of viral replication by JAK1-inhibitor ruxolitinib in Calu-3 cells at 48 h.p.i., where relative infection levels are shown across three independent experiments determined by E copies per microgram RNA normalized to the median infection level of the untreated control (**g**). **h–k.** Primary bronchial HAEs were infected with the indicated

variants at 1,500 E copies per cell: viral replication measured by intracellular E copies at 72 h.p.i. (**h**) and viral release into apical washes over time (**i**), with three biological replicates shown; expression of *IFNB*, *CXCL10*, *IFIT1*, *IFIT2*, *DDX58* and *RSAD2* in HAEs at 72 h.p.i., with six biological replicates shown (**j**); intracellular viral E copies in HAEs in the presence or absence of 5 μM ruxolitinib at 72 h.p.i., with three biological replicates shown (**k**). For **a**, one-way analysis of variance (ANOVA) with Bonferroni post-test was used. n.s., not significant at $P > 0.05$ for all comparisons. For **b–h** and **j**, one-way ANOVA and Dunnett’s post-test were used. For **i**, two-way ANOVA with a Bonferroni post-test was used. For **k**, one-tailed unpaired Student’s *t*-test was used. Replicate measurements from one of three independent experiments. Fold change over mock is shown. Mean ± s.e.m. or individual datapoints are shown. h.p.i., hours post infection.

are also accumulating mutations beyond spike^{17,18}, suggesting that spike-independent adaptations may also be crucial for Omicron variant dominance. In this Article, we provide evidence that, similar to VOCs Alpha to Delta, Omicron variants also improve innate immune evasion through enhancement of viral protein expression, suggesting that regulation of host responses through adapting viral protein levels is a key feature of SARS-CoV-2 evolution.

Results

To understand phenotypic differences between Omicron subvariants, and the selective forces driving their evolution, we compared replication of, and host responses to, BA.1–BA.5 with Delta, the previously dominant VOC, in Calu-3 human airway epithelial cells (HAEs; Fig. 1).

We equalized input dose of each variant by viral envelope (E) gene copies (quantitative reverse transcription polymerase chain reaction, RT–qPCR) as this ensures cells are exposed to equal starting amounts of viral RNA, which is the major viral PAMP activating defensive host innate immune responses^{1,19}. Most importantly, this approach normalizes dose independently of variant-specific differences in cell tropism or entry routes (Fig. 1a and Extended Data Fig. 1a,b)^{20–22}, which we and others have shown impact both titre determination and input equalization by cell-line infectivity measurements such as 50% tissue culture infectious dose (TCID₅₀) or plaque assay (Extended Data Fig. 1c–e). Our approach is particularly relevant for comparing Omicron subvariants because Omicron spike mutations have been shown to alter tropism, increasing cathepsin-dependent endosomal entry and reducing dependence on

cell surface TMPRSS2 (refs. 20–23), irrespective of virion spike cleavage efficiency (Extended Data Fig. 1f). Endosomal cathepsins or cell surface TMPRSS2 are required to cleave spike before ACE2-mediated entry^{24,25}. Indeed, in line with previously published data^{20–22}, we have found that Omicron, particularly BA.5, has enhanced entry (cathepsin dependent and E64d sensitive) in TMPRSS2-negative cells such as Hela-ACE2 compared with previous VOCs such as Delta, whereas entry into Calu-3 cells is largely TMPRSS2 dependent (camostat sensitive) (Extended Data Fig. 1a,b), resulting in striking cell type-specific differences between variant titres by TCID₅₀ (Extended Data Fig. 1e).

Infection of Calu-3 cells with 2,000 E gene copies per cell (Fig. 1) or 200 E copies per cell (Extended Data Fig. 1) gave comparable E RNA (RT-qPCR) at 2 h post infection (h.p.i.), consistent with equal input doses (Fig. 1a and Extended Data Fig. 1g). E gene measurements during infection revealed that Omicron isolates BA.1, BA.2, BA.4 and BA.5 replicated similarly, lagging behind Delta in Calu-3 cells (Fig. 1b and Extended Data Fig. 1h–l). BA.4 replicated most slowly initially but caught up with BA.1, BA.2 and BA.5 by 24 h.p.i. (Fig. 1b and Extended Data Fig. 1). Importantly, these replication differences were observed consistently across several experiments (Fig. 1 and Extended Data Figs. 1 and 2). As E gene measurement during infection captures genomic RNA (gRNA) as well as E, S and Orf3 subgenomic RNAs (sgRNAs), we compared the levels of intracellular E RNA with those of Nsp12 and Orf1a (compare Extended Data Fig. 1h,i with Fig. 1b and Extended Data Fig. 1k,l with Extended Data Fig. 1j), which are uniquely encoded within gRNA. Importantly, the ratio of E to Nsp12 was similar until 24 h.p.i. reflecting equivalent levels of E sgRNA synthesis between variants (Extended Data Fig. 1m). Quantification of released virions by measuring E and Nsp12 RNA copies in the supernatant mirrored viral replication (Extended Data Fig. 1n–q). Similar patterns of infection were also seen when quantified by intracellular nucleocapsid (N) staining (Fig. 1c and Extended Data Fig. 1r).

BA.4 and BA.5 trigger less innate immune activation than earliest Omicron subvariants

We next compared the host innate immune response to Omicron subvariant infection of Calu-3 cells. All viral stocks were prepared in human gastrointestinal Caco-2 cells as they are naturally permissive to SARS-CoV-2 replication but do not mount a strong innate response to this infection^{19,26}. We confirmed that viral stocks prepared in Caco-2 cells (the highest viral inoculum for each variant was 2,000 E copies per cell) did not contain measurable interferon (IFN) β and negligible IFN λ 1/IFN λ 3 (enzyme-linked immunosorbent assay, ELISA) (Extended Data Fig. 2a,b), ensuring differences in innate immune activation in Calu-3 infections were not a result of IFN carryover in the viral stocks.

Strikingly, we found that infection of Calu-3 cells with BA.4 and BA.5 resulted in significantly less innate immune activation compared to BA.1/BA.2, evidenced by lower induction of IFN β (*IFNB*) and interferon stimulated genes (ISGs) including inflammatory chemokine *CXCL10* and *RSAD2*, *DDX58*, *IFIT1* and *IFIT2* (Fig. 1d and Extended Data Fig. 2c–g) and a trend towards reduced *MX1* and *MX2* expression (Fig. 1d). Reduced host responses to BA.4 and BA.5 infection were also evident at the level of IFN β and *CXCL10* secretion (Fig. 1e,f). Slower replication of BA.4 probably contributes in part to reduced innate immune activation during Calu-3 infection, but BA.5 replication was similar to BA.1 and BA.2 and nonetheless induced significantly less innate immune responses. Inhibition of IFN-mediated JAK/STAT signalling with ruxolitinib, evidenced by the absence of ISG induction (Extended Data Fig. 2e,f), rescued BA.1 and BA.2 infection in Calu-3 cells to a greater degree than BA.4 or BA.5 (Fig. 1g and Extended Data Fig. 2h–j), suggesting that the greater induction of IFN β by BA.1 and BA.2 reduced their infectivity. BA.1 to BA.5 showed similar sensitivities to a range of IFN doses used to pre-treat Calu-3 cells (Extended Data Fig. 2k–m). We therefore conclude that the differences in ruxolitinib sensitivity reflect differences in IFN induction after Calu-3 infection

and not differences in IFN sensitivity. Infecting Calu-3 cells with lower virus input doses (200 E copies per cell) recapitulated our observation that Delta replicated better than Omicron BA.1–BA.5 (Extended Data Fig. 1j–l), and we again saw reduced innate immune activation by BA.4 and BA.5 compared with BA.1 and BA.2 (Extended Data Fig. 2f,g). At this lower inoculum, BA.4 infectivity was also strongly rescued by ruxolitinib treatment consistent with its slower replication being due to IFN induction (Extended Data Fig. 2i).

We next compared Omicron subvariant replication and host responses in primary HAE cultures, which better recapitulate the heterogeneous polarized epithelial layer of the respiratory tract. We have previously reported that HAEs reveal differences in VOC replication that probably reflect host adaptation, which are not always apparent in highly permissive cell lines, such as Calu-3 (refs. 1,2). Concordantly, BA.5 viral replication was higher than BA.2 and BA.4 in differentiated primary bronchial HAEs at 72 h.p.i., while apical viral release over time was comparable (Fig. 1h,i). Despite BA.4 and BA.5 replicating similarly to BA.2 in HAEs, we consistently observed reduced innate activation, measured by ISG induction, after BA.4 and BA.5 infection (*IFNB*, *CXCL10*, *IFIT1*, *IFIT2*, *DDX58* and *RSAD2*; Fig. 1j). Inhibiting IFN signalling with JAK-inhibitor ruxolitinib suppressed ISG induction (Fig. 1j) and rescued replication of BA.2 to a greater degree than BA.4 and BA.5 (Fig. 1k). Altogether, data in Fig. 1 suggest adaptation to reduce innate immune activation between the earliest (BA.1 and BA.2) and subsequent (BA.4 and BA.5) Omicron subvariants.

SARS-CoV-2, and other respiratory viruses, reportedly replicate more efficiently in nasal and tracheal epithelial cells²⁷, in part due to reduced innate activation and IFN responsiveness at the lower temperatures of the upper airway^{28–30}. To investigate whether lower temperatures reveal further Omicron subvariant adaptation, we compared replication at 32 °C in Calu-3 cells. We found BA.1 to BA.5 all replicated less well than at 37 °C (Extended Data Fig. 3a,b) whereas Delta replication was not as temperature sensitive. As expected²⁹, innate immune activation in response to infection, or to RNA sensing agonist poly(I:C), was largely abolished at 32 °C (measured by *IFNB* and *CXCL10* messenger RNA induction; Extended Data Fig. 3c–e). At 37 °C, we again observed lower innate activation for BA.4 and BA.5 compared with BA.1/BA.2. In HAE, lowering the temperature to 32 °C did not impact viral replication to the same extent as in Calu-3 cells (Extended Data Fig. 3f). However, we observed reduced virus output in apical washes from infected HAE cultures for all Omicron isolates (Extended Data Fig. 3g–i). Infected HAEs at 32 °C also expressed significantly less *IFNB* and *CXCL10* (Extended Data Fig. 3j). Overall, our data suggest that Omicron does not replicate better at 32 °C in lung epithelial cells even in the absence of an innate immune response. However, it is possible that the intra-tissue temperature throughout the airways remains closer to 37 °C than the exhaled breath temperature of 32 °C suggests³¹.

BA.4 and BA.5 increase Orf6 expression and efficiently antagonize innate immune activation during infection

We next investigated the mechanism underlying differential innate immune activation by Omicron subvariants. IRF3 and STAT1 are key transcription factors responding to intracellular RNA sensing and IFN production, respectively, exemplified here by poly(I:C) treatment (Extended Data Fig. 4a–c). We and others have shown that SARS-CoV-2 activates transcription factors IRF3 and STAT1 downstream of RNA sensing^{19,32}. Consistent with their reduced innate immune triggering, we found Omicron BA.4 and BA.5 infection activated significantly less IRF3 phosphorylation than BA.2 infection (Fig. 2a–c). A similar trend was observed for STAT1 serine 727 phosphorylation, which is essential for full STAT1 transcriptional activity³³, but not upstream JAK1-dependent tyrosine 701 phosphorylation (Fig. 2a,d–f). Reduction of STAT1 phosphorylation correlated with reduced STAT1 nuclear translocation during BA.4 and BA.5 infection compared with BA.2, measured by high-content single-cell immunofluorescence imaging of infected

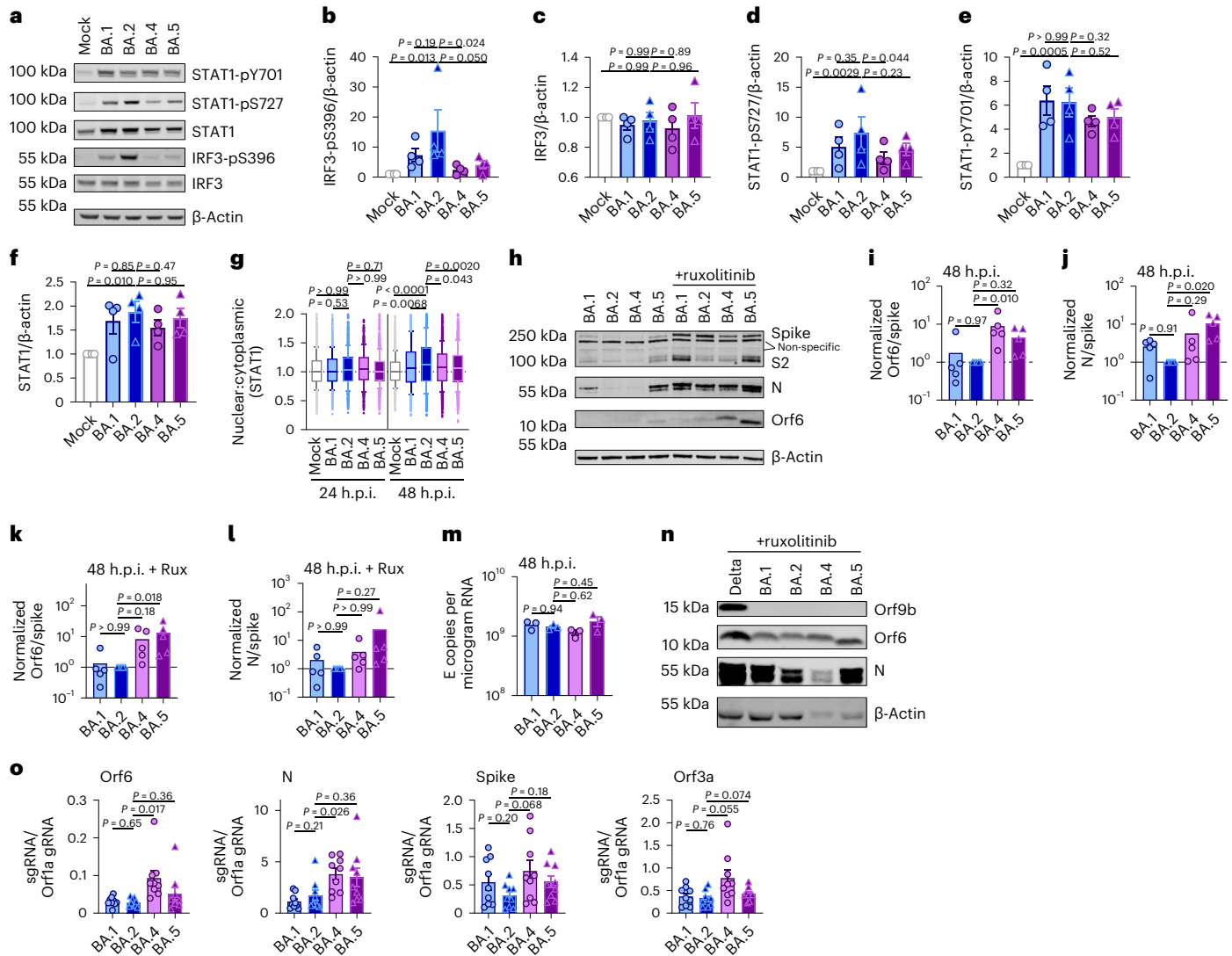


Fig. 2 | BA.5 efficiently expresses SARS-CoV-2 innate antagonists during airway epithelial cell infection. Calu-3 cells were infected with 2,000 E copies per cell of the indicated variants. **a**, Western blot of STAT1-pY701, STAT1-pS727, total STAT1, IRF3-pS396, total IRF3 and β-actin at 24 h.p.i. One of four independent western blots is shown. **b–f**, Quantification of four independent western blots showing IRF3-pS396 (**b**), IRF3 (**c**), STAT1-pS727 (**d**), STAT1-pY701 (**e**) and STAT1 (**f**) over β-actin at 24 h.p.i. normalized to mock. **g**, Quantification of STAT1 nuclear translocation detected by single-cell fluorescence microscopy over time in Calu-3 cells infected with the indicated variants. Data from 1,500 cells per condition are shown. In infected cultures, translocation was determined in N+ cells. **h**, Western blot of Orf6, N, spike and β-actin at 48 h.p.i. in infected cells ± 5 μM ruxolitinib (Rux). Non-specific bands detected by polyclonal anti-spike primary antibody are indicated (see Extended Data Fig. 4e for mock).

One of five independent western blots shown. **i–l**, Quantification of Orf6 and N expression from five independent western blots of Calu-3 cells in the absence (**i**, Orf6; **j**, N) or presence of 5 μM ruxolitinib (**k**, Orf6; **l**, N) at 48 h.p.i., normalized to spike over BA.2. **m**, Viral replication in cells from **h**, **n**, Representative western blot of Calu-3 cells infected with Delta, BA.1, BA.2, BA.4 and BA.5 at 2,000 E copies per cell showing Orf9b, Orf6, N and β-actin expression at 48 h.p.i. + 5 μM ruxolitinib. **o**, sgRNA expression of Orf6, N, spike and Orf3a normalized to Orf1a gRNA in Calu-3 cells at 48 h.p.i.; nine measurements from three independent experiments shown. For **b–f**, **i–m** and **o**, one-way analysis of variance with Dunnett’s post-test was used. For **g**, box-and-whisker blots show 10th–90th percentile, and groups were compared at each timepoint as indicated using a Kruskal–Wallis test. Mean ± s.e.m. or individual datapoints are shown.

nucleocapsid-positive Calu-3 cells (Fig. 2g). These data suggest that BA.4 and BA.5 more effectively prevent intracellular activation of innate sensing pathways. We previously reported that SARS-CoV-2 VOC Alpha evolved enhanced innate immune evasion by increasing expression of key innate antagonists Orf6, Orf9b and N (Extended Data Fig. 4d), which manipulate host cell innate immune pathways¹. To investigate whether Omicron subvariants have also independently evolved enhanced innate immune suppression through similar mechanisms during human adaptation, we measured viral innate antagonist protein expression during infection. Strikingly, we found that BA.4, and particularly BA.5, expressed higher levels of Orf6 and N compared with BA.1 and BA.2 (Fig. 2h–l and Extended Data Fig. 4e–k), measured at 48 h.p.i. in

Calu-3 cells when ERNA levels were equivalent (Fig. 2m). Unlike previous VOCs^{1,2}, expression of innate immune antagonist Orf9b was not detected for any Omicron isolate, possibly due to Omicron subvariants encoding lineage-specific Orf9b mutations (P10S and ΔENA at positions 27–29) altering antibody binding and precluding detection by immunoblot (Fig. 2n and Extended Data Fig. 4d). Importantly, Orf9b remained readily detectable in Delta-infected cells (Fig. 2n). Upregulation of Orf6 and N expression by BA.5 was validated using a second independent isolate (Extended Data Fig. 4l–n), and was also evident in lysates from infected HAEs (Extended Data Fig. 4o). Blocking IFN signalling with ruxolitinib rescued replication of all Omicron isolates as before (Fig. 1 and Extended Data Fig. 2) and enhanced viral protein detection by

immunoblot (Fig. 2h,n and Extended Data Fig. 4e). Importantly, higher levels of BA.4 and BA.5 Orf6 and N remained apparent after ruxolitinib treatment (Fig. 2h,k,l). We previously showed that enhanced levels of Orf6, N and Orf9b protein by Alpha were associated with increased levels of the corresponding sgRNAs¹. By contrast, BA.5 Orf6 and N sgRNA levels (normalized to genomic Orf1a) were not enhanced, and were only slightly upregulated during BA.4 infection (Fig. 2o), particularly in comparison with Alpha (Extended Data Fig. 4p,q). No differences were observed in S and Orf3a sgRNAs, which served as controls to rule out a general enhancement of sgRNA synthesis (Fig. 2o). Although Omicron subvariants have synonymous and non-synonymous mutations in Orf6 and N, there are no mutations that distinguish BA.4 and BA.5 from BA.1 and BA.2 that provide a simple explanation for increased Orf6 or N protein levels, including in their transcriptional regulatory sequences (Figs. 1 and 2 and Extended Data Tables 1 and 2). Thus, we hypothesize that BA.4 and BA.5 have either evolved independent mechanisms to increase Orf6 and N protein levels, or that the increase is mediated by changes elsewhere in the genome, which may impact viral translation or protein stability. Further studies are required to pinpoint the adaptations regulating Orf6 and N expression levels.

Orf6 expression is a major determinant of enhanced innate immune antagonism by emerging VOCs

Orf6 is a multifunctional viral accessory protein that modulates expression of host and viral proteins^{34,35}. Orf6 selectively inhibits host transcription factor nuclear transport to potentially antagonize antiviral responses during infection. To probe Orf6 mechanisms, and its contribution to enhanced innate antagonism by the VOCs, we used reverse genetics to introduce two stop codons into the Orf6 coding sequence of both Alpha (Alpha Δ Orf6) and BA.5 (BA.5 Δ Orf6), which we confirmed abolished Orf6 expression during infection (Fig. 3a,b). While Alpha Δ Orf6 replicated similarly to parental wild-type (WT) virus up to 24 h.p.i. (Fig. 3c), we observed enhanced *IFNB* and *CXCL10* expression (Fig. 3d) and protein secretion (Extended Data Fig. 5a) during Alpha Δ Orf6 infection of Calu-3 cells compared with WT virus. Moreover, increased IRF3 nuclear translocation was evident after Alpha Δ Orf6 infection at 24 h.p.i. using single-cell quantitative immunofluorescence microscopy (Fig. 3e and Extended Data Fig. 5b). This suggests an important role for Orf6 in innate immune antagonism during viral replication^{1,35–37} and is consistent with suppression of IRF3 nuclear transport in Orf6 overexpression studies^{35,36,38}. The reduction in Alpha Δ Orf6 replication at 48 h.p.i., and N and spike protein expression at 24 h.p.i., that was rescued by ruxolitinib treatment, is also consistent with greater IFN-mediated suppression of the Orf6 deletion mutant (Fig. 3a and Extended Data Fig. 5c).

Alpha Δ Orf6 also replicated less well than WT in HAE cells (Fig. 3f–h and Extended Data Fig. 5d). *IFNB* and *CXCL10* gene induction, normalized to *GAPDH*, were similar after Alpha Δ Orf6 and WT infection (Fig. 3i), despite lower E RNA levels for Alpha Δ Orf6, consistent with increased innate immune induction by the deletion virus. Importantly, Alpha Δ Orf6 was more sensitive to ruxolitinib treatment than WT, consistent with the notion that increased IFN induction caused reduced replication of Alpha Δ Orf6 (Fig. 3g,h). To address the role of Orf6 during BA.5 infection, we compared replication of a BA.5 Δ Orf6 mutant with parental BA.5 WT virus. We also generated a BA.5 mutant bearing the Orf6 D61L mutation found in BA.2 and BA.4 that has been proposed to reduce Orf6 function^{2,32,39} (Fig. 3b,j). Consistent with the SARS-CoV-2 Alpha Δ Orf6 results, BA.5 Δ Orf6 showed a replication defect at 48 h.p.i. compared with BA.5 WT, and triggered significantly enhanced innate immune responses evidenced by enhanced *IFNB* and ISG induction (Fig. 3k,l). Deletion of Orf6 in BA.5 also increased the degree of infection-induced IRF3 and STAT1 phosphorylation (Fig. 3m–r) and nuclear translocation (Fig. 3s,t). This demonstrates that Orf6 loss enhances IRF3 and STAT1 activation despite similar levels of infection in the first 24 h.p.i., confirming the important role of Orf6 in innate

immune suppression and in distinguishing BA.5 from earlier Omicron subvariants. Infection of HAEs confirmed reduced viral replication of BA.5 Δ Orf6 compared with WT BA.5, while viral release remained comparable (Fig. 3u,v and Extended Data Fig. 5e). ISG expression in HAEs was similar between WT and mutant despite lower E RNA levels during BA.5 Δ Orf6 infection, suggesting greater induction of innate immunity in the absence of Orf6 in these cells (Extended Data Fig. 5f). Interestingly, introducing the C-terminal D61L mutation into BA.5 Orf6 resulted in an intermediate innate immune phenotype measured by increased induction of *IFNB*, *CXCL10* and *IFIT1* expression by the mutant virus (Fig. 3l). IRF3 phosphorylation and nuclear translocation were equivalent between BA.5 WT and Orf6 D61L (Fig. 3n–s), whereas STAT1 translocation was not antagonized by Orf6 D61L (Fig. 3t), in line with reports of a partial loss of Orf6 function in the D61L mutation^{2,32,39}. These data suggest complex adaptation of Orf6 manipulation of innate immunity during SARS-CoV-2 Omicron lineage adaptation.

Enhanced innate antagonism is a conserved feature of dominant Omicron subvariants

During the course of this study, SARS-CoV-2 has continued to evolve and produce new Omicron subvariants (Fig. 4a and Extended Data Fig. 6a). Omicron subvariants BA.2.75, XBB.1, XBB.1.5 and BQ.1.1 have acquired increased ACE2 binding and enhanced adaptive immune evasion^{40–43}. To test whether enhanced innate immune antagonism is consistently associated with globally successful subvariants, we compared BA.2.75, XBB.1, XBB.1.5 and BQ.1.1 isolates with BA.2 and BA.5 (Fig. 4). We equalized virus dose by Nsp12 RNA copies (RT–qPCR), a measurement of gRNA, rather than E RNA copies, due to accumulation of mutations in the E gene of later Omicron subvariants, including in the region detected by our RT–qPCR assay. We found that all Omicron subvariants retained an enhanced dependence on cathepsin, here measured in A549 cells expressing ACE2 and TMPRSS2 (Extended Data Fig. 6b). BA.2.75, XBB.1 (two independent isolates) and XBB.1.5, derived from the parental BA.2 lineage^{41,43}, replicated comparably to earlier BA.2 and BA.5 in Calu-3 and HAEs (Fig. 4b–e and Extended Data Fig. 6c–h). BQ.1.1, which has arisen from BA.5 (ref. 43), displayed some reduction of replication in epithelial cells (Fig. 4d,e and Extended Data Fig. 6e,h). Similar to BA.5, we found that all subsequent Omicron subvariants tested triggered significantly less *IFNB* and *CXCL10* expression than BA.2 at 24 h.p.i. (Fig. 4f). All Omicron subvariants derived from BA.2 (BA.2.75, XBB.1 and XBB.1.5) showed reduced rescue by ruxolitinib treatment, as well as reduced induction of, or sensitivity to, IFN, similar to BA.5 (Fig. 4g and Extended Data Fig. 6i). Strikingly, like BA.5, enhanced innate immune evasion by these more recent subvariants was accompanied by increased Orf6 expression for the majority of isolates (Fig. 4h,i). Reduced BQ.1.1 replication in Calu-3 cells (Fig. 4d and Extended Data Fig. 6e) prevented Orf6 and N detection in the absence of ruxolitinib (Fig. 4h). Reduced innate activation by recent Omicron subvariants also correlated with reduced IRF3 phosphorylation compared with BA.2, and reduction of STAT1 serine phosphorylation was principally observed for XBB.1 and XBB.1.5 variants (Fig. 4j–l and Extended Data Fig. 6j–l). Together these data are consistent with a trend for ongoing Omicron evolution enhancing Orf6 expression as it adapts to the human population leading to reduced innate immune responses, detectable at the level of IFN and ISG expression, and at the level of transcription factor phosphorylation and nuclear translocation. This study considering Omicron variants is very reminiscent of our previous observation of enhanced expression of key innate immune antagonists Orf6, N and Orf9b in VOCs Alpha to Delta suggesting a common evolutionary trajectory to combatting human innate immunity to enhance transmission^{1,2}.

Discussion

We propose a model in which the earliest host innate immune responses make an important contribution to SARS-CoV-2 transmission by influencing whether interactions with the first few cells in

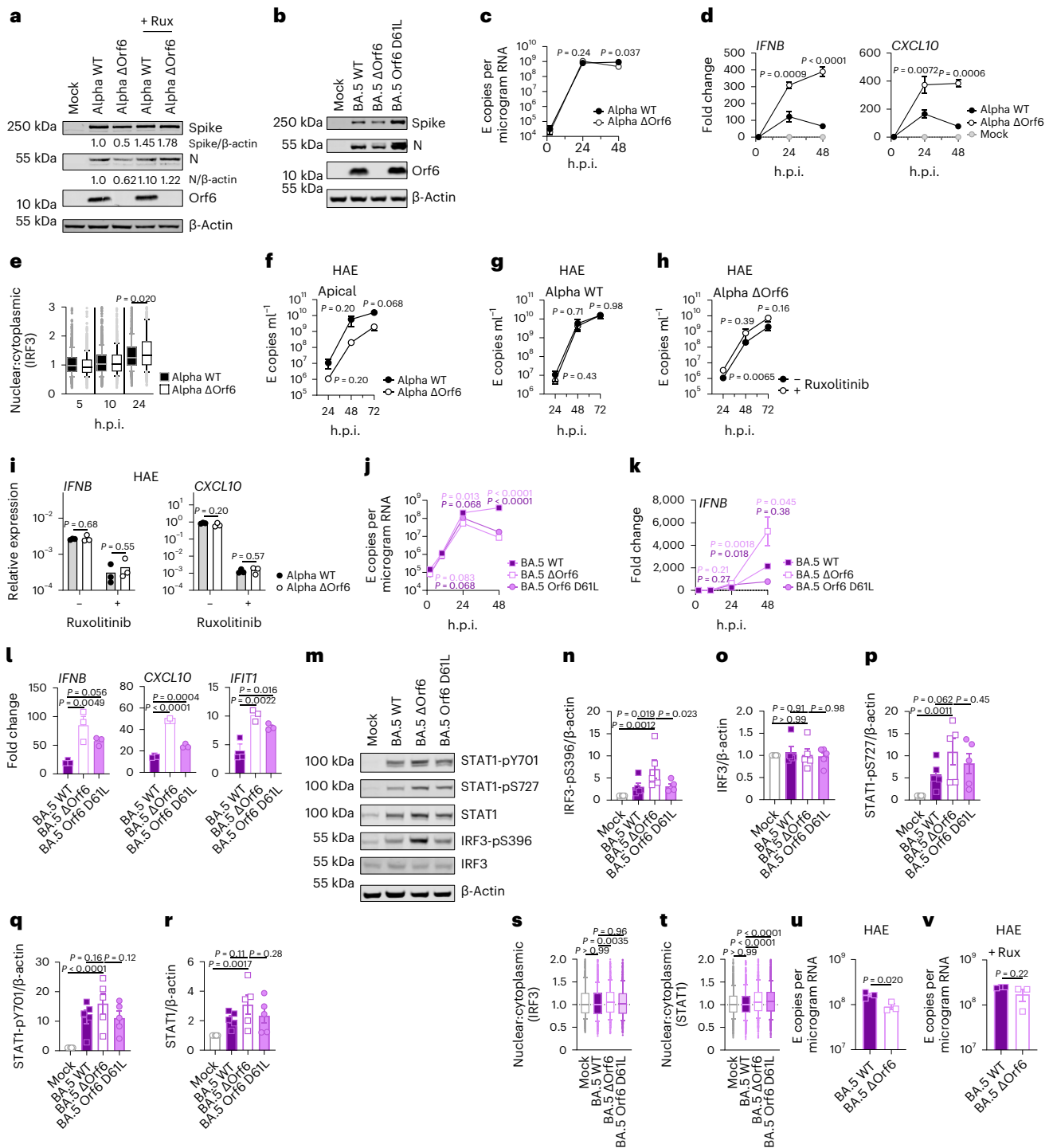


Fig. 3 | Orf6 expression is a major determinant of enhanced innate immune antagonism by emerging VOCs. a, b, Western blot of Alpha (a) or BA.5 (b) reverse genetic (RG) virus infections in Calu-3 cells at 24 h.p.i. ± 5 μM ruxolitinib (Rux). **c**, Replication of RG viruses parental Alpha WT and ΔOrf6 in Calu-3 cells infected with 2,000 E copies per cell over time. **d**, Gene expression in cells from over time. **e**, Quantification of IRF3 nuclear translocation detected by single-cell fluorescence microscopy over time. **f–i**, HAEs were infected with 1,500 E copies per cell of the indicated variants ± 5 μM ruxolitinib. **f**, Viral release into apical washes over time. **g,h**, Apical release in HAEs infected with Alpha WT (g) or ΔOrf6 ± 5 μM ruxolitinib (h). **i**, Gene expression in cells from f. Three biological replicates shown. **j**, Replication of RG viruses BA.5 WT, ΔOrf6 and Orf6 D61L isolates in Calu-3 cells infected with 2,000 E copies per cell over time. **k**, *IFNB* expression in cells from j. **l**, Gene expression of Calu-3 cells at 24 h.p.i. **m**, Western blot of STAT1-pY701, STAT1-pS727, total STAT1, IRF3-pS396, total

IRF3 and β-actin at 24 h.p.i. **n–r**, Quantification of five independent western blots showing IRF3-pS396 (n), total IRF3 (o), STAT1-pS727 (p), STAT1-pY701 (q) and total STAT1 (r) over β-actin at 24 h.p.i. **s, t**, Quantification of IRF3 (s) and STAT1 (t) nuclear translocation detected by single-cell fluorescence microscopy at 24 h.p.i. **u, v**, Replication of BA.5 WT and ΔOrf6 in HAEs infected with 1,500 E copies per cell in the absence (u) or presence (v) of 5 μM ruxolitinib. For c and d, two-way analysis of variance (ANOVA) and Bonferroni post-test were used. For e, s and t, data from 1,500 cells per condition are shown as box-and-whisker blots indicating 10th–90th percentile. In infected cultures, translocation was determined in N+ cells. Groups were compared by Kruskal–Wallis test. For k, l and n–r, one-way ANOVA with Dunnett’s post-test was used. For f–i, u and v, unpaired two-tailed Student’s *t*-test was used. Replicate measurements from one of three independent experiments. Fold change over mock is shown. Mean ± s.e.m. or individual datapoints are shown.

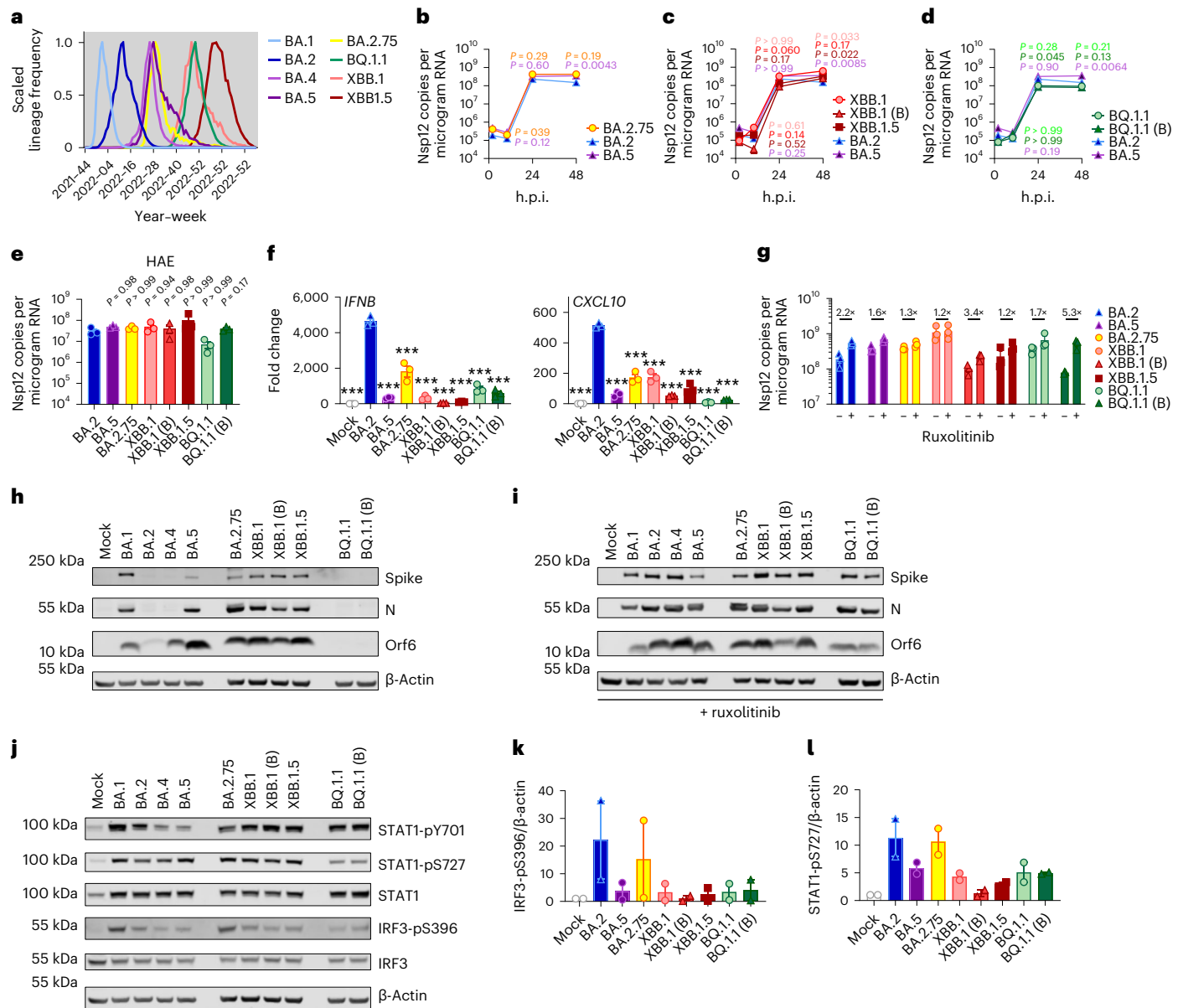


Fig. 4 | Innate immune phenotype of dominant Omicron subvariants.
a, Global SARS-CoV-2 variant sequence counts over time (scaled per variant), extracted from CoV-Spectrum using genomic data from GISAID. **b–d**, Calu-3 cells were infected with 2,000 Nsp12 copies per cell. Replication of Omicron subvariants compared with BA.2 (blue) and BA.5 (purple) measured by Nsp12 copies per microgram RNA is shown for BA.2.75 (yellow; O) (**b**), XBB subvariants (XBB.1: light red, O; XBB.1 (B): red, Δ; XBB.1.5: dark red, □) (**c**) and BQ.1.1 (BQ.1.1: light green, O; BQ.1.1 (B): dark green, Δ) (**d**) isolates. **e**, HAEs were infected with 1,500 Nsp12 copies per cell and intracellular Nsp12 copies measured at 72 h.p.i. Three biological replicates shown. **f**, *IFNB* and *CXCL10* expression in Calu-3 cells infected with 2,000 Nsp12 copies per cell of the indicated Omicron subvariants at 24 h.p.i. **g**, Viral replication of indicated variants in Calu-3 cells in the presence or absence of 5 μM ruxolitinib at 48 h.p.i. Numbers indicate fold change in

replication in the presence of 5 μM ruxolitinib. **h, i**, Western blot of Orf6, N, spike and β-actin at 48 h.p.i. in cells from **b–d** in the absence (**h**) or presence (**i**) of 5 μM ruxolitinib. **j**, Western blot of STAT1-pY701, STAT1-pS727, total STAT1, IRF3-pS396, total IRF3 and β-actin in Calu-3 cells at 48 h.p.i. **k, l**, Quantification of two independent western blots of IRF3-pS396 (**k**) and STAT1-pS727 (**l**) over β-actin at 24 h.p.i. For **b–d**, variant replication was compared with BA.2 at each timepoint using a two-way analysis of variance (ANOVA) and Bonferroni post-test. Colours indicate comparator (BA.5, purple; BA.2.75, yellow; XBB.1, light red; XBB.1 (B), red; XBB.1.5, dark red; BQ.1.1, light green; BQ.1.1 (B), dark green). For **e–g**, one-way ANOVA with Dunnett’s post-test was used to compare all variants with BA.2. Replicate measurements from one of three independent experiments. Fold change over mock is shown. Mean ± s.e.m. or individual datapoints are shown. For **f**, ****P* < 0.0001.

the airway establish a productive infection. In this model, viruses with enhanced ability to evade or antagonize innate immunity, for example, through increased Orf6 and N expression, will transmit with greater frequency because they are better at avoiding inducing, or better at shutting down, the host responses that suppress this earliest replication. This model is supported by longitudinal nasal sampling of SARS-CoV-2-infected patients shortly after confirmation of infection, which revealed pronounced and early upregulation of an

innate immune response in epithelial cells that rapidly declines after symptom onset⁴⁴.

How early viral manipulation of the host innate immune response influences disease is less clear. We hypothesize that, once infection of the airway is irrevocably established, innate immune suppression that permits greater levels of viral replication may in turn lead to increased disease, simply due to greater viral burden and greater inflammatory responses. Concordantly, higher baseline antiviral gene expression

and more potent innate induction in the nasal epithelium of children are associated with less severe infection outcomes compared with adults⁴⁵. Like others, we assume this is explained by reduced viral loads reducing disease and early IFN protecting against transmission, with late IFN responses contributing to disease⁴⁶. Similarly, inborn errors of innate antiviral mechanisms and IFN autoantibodies are associated with severe coronavirus disease 2019 (COVID-19)^{47–51}, assumed to be explained by greater viral loads driving increased inflammatory disease. Furthermore, clinical trials of JAK/STAT inhibitors reduced COVID-19 mortality after hospitalization⁵². Considering an unrelated virus, simian immunodeficiency virus in macaques, may be relevant. Here transmission efficiency and subsequent disease are also influenced by IFN at the site of infection⁵³. In all these examples, early IFN is beneficial, reducing transmission, but late IFN is bad, increasing symptoms. Human SARS-CoV-2 challenge studies are expected to help us understand the effect of these dynamics and innate immune contributions to transmission and disease by permitting sampling before exposure and during the earliest timepoints post infection with careful assessment of disease in a highly controlled environment^{54,55}.

We have focused on changes in expression of N and Orf6 but we expect that other viral genes contribute to evasion of innate immunity and adaptation to humans. In contrast to common cold coronaviruses, SARS-CoV-2 and its relatives encode a broad range of accessory genes^{56,57} that antagonize innate immunity and probably contribute to effective transmission between species. Our data suggest that upregulation of Orf6 expression is a central feature of SARS-CoV-2 adaptation to humans. Our observations using Orf6-deletion viruses confirm Orf6 to be a potent viral innate immune antagonist, as reported by others^{32,34,35,39}, and are consistent with a model in which, like Alpha, Omicron subvariant enhancement of Orf6 expression contributes to the reduced innate immune response to infection compared with earlier Omicron viruses. Orf6 upregulation by BA.5 may, in part, explain increased pathogenicity *in vivo*³⁴. This notion is supported by Δ Orf6 SARS-CoV-2 infection of transgenic mice or hamsters, where the Orf6 mutant causes less severe disease and there is quicker recovery from infection, despite comparable viral loads in nose and lungs^{32,58}. Expression of accessory and structural proteins as sgRNAs during SARS-CoV-2 replication provides an elegant mechanism to selectively regulate their abundance during adaptation to host, as the level of each sgRNA and thus protein can be independently adjusted by mutation, as we found for VOCs Alpha to Delta^{1,2}.

The earliest Omicron subvariants BA.1 and BA.2 outcompeted Delta despite not enhancing innate immune antagonism, explained by extensive antibody escape^{1–14} and improved spike function/stability^{59,60}. This suggests that adaptive immunity was the strongest selection force for Omicron emergence and global dominance. We hypothesize that the acquisition of enhanced innate immune suppression by Omicron lineage variants after their initial emergence required selection for improved transmission and dominance. Thus, innate immune escape may be the second dominant selective force the virus experiences after escape from neutralizing antibodies in a population with pre-existing immunity from prior infection and vaccination. We propose that evolving to better manage host innate immunity for improved transmission is a central feature of species-specific host adaptation for all emerging viruses. Intriguingly, SARS-CoV-2 continues to jump species barriers and has been detected infecting 34 different animal species so far⁶¹, illustrating its remarkable capacity to universally antagonize species specific innate immune responses. SARS-CoV-2 will be a fantastic model to further dissect species barriers to zoonotic spillovers and understand how viruses adapt to new species.

We propose that adaptation in spike and beyond also contributes to enhanced replication in human cells^{1,2}. This may be important for outpacing early innate responses during transmission particularly in environments with a mix of permissive and non-permissive cells such as the upper human airways in which ACE2 is expressed only on ciliated

cells⁶². Indeed, we have found that SARS-CoV-2 replicates more slowly in primary HAE cultures than in Calu-3 cells and that HAEs better recapitulate VOC replication advantages^{1,2}. Primary HAEs complement more tractable monoculture models, such as Calu-3 that allow mechanistic studies. We propose that linking VOC genotype to phenotype in multiple models will be essential for effective prediction of novel variant behaviour. Moreover, understanding how adaptive changes in spike, leading to altered viral tropism, influence innate immune responses also warrants further study.

This study adds to the body of evidence for innate immunity being a key barrier that must be overcome by all pandemic zoonotic viruses, particularly in the absence of immune memory in an exposure-naive species. This has also been elegantly demonstrated recently for influenza virus where avian, but not human influenza virus, is efficiently restricted by human BTN3A3 (ref. 63), which like MX1 (ref. 64) can be overcome by adaptation to the human host. Innate immune evasion has also been linked to the single pandemic human immunodeficiency virus-1 lineage⁶⁵. Our findings herein have broad implications for understanding zoonotic pathogen emergence because they reveal molecular details of how SARS-CoV-2 Omicron subvariants have achieved dominance, unexpectedly by increasing specific protein expression rather than adapting by protein coding mutation. Crucially, they suggest that improvements in innate immune evasion can continue to enhance transmission, even after establishment in humans. We hypothesize an inevitable ongoing trajectory of adaptation towards escape from the innate immune mechanisms that are the gatekeepers of transmission success.

Methods

Cell culture

Calu-3 cells were purchased from AddexBio (C0016001), Caco-2 cells were a kind gift from Dalan Bailey (Pirbright Institute), Hela-ACE2 cells were a gift from James E. Voss⁶⁶ and A459 cells expressing ACE2 and TMPRSS2 were previously described²². Cell lines were cultured in Dulbecco's modified Eagle medium (DMEM) supplemented with 10% heat-inactivated foetal bovine serum (FBS, Labtech) and 100 U ml⁻¹ penicillin–streptomycin. Cells were passaged at 80–90% confluence. For infections, Calu-3 and Caco-2 cells were seeded at 2×10^5 cells ml⁻¹ and Hela-ACE2 cells at 1×10^5 cells ml⁻¹ and grown to 60–80% confluence for experiments^{1,19}. Primary normal (healthy) bronchial epithelial (NHBE-A) cells from two independent donors were cultured for five to seven passages and differentiated at an air–liquid interface as previously described¹. After 21–24 days of differentiation, cells were used in infection experiments. Experiments were performed without blinding or randomization.

Viruses

SARS-CoV-2 lineages Alpha (B.1.1.7), Delta (B.1.617.2)²¹ and Omicron (lineage B.1.1.529.1/BA.1, lineage B.1.1.529.2/BA.2, lineage BA.2.75 (BA.2.75.3) lineage BQ.1.1 (BQ.1.1.1), lineage XBB.1) isolates were a gift from Wendy Barclay (Imperial College London, United Kingdom). Omicron BA.4 (lineage B.1.1.529.4), BA.5 (lineage B.1.1.529.5), BQ.1.1 (B) (BQ.1.1.15) and lineage XBB.1.5 (XBB.1.5.13) were a gift from Alex Sigal and Khadija Khan (Africa Health Research Institute, Durban, South Africa)^{7,14}. SARS-CoV-2 BA.5 (B) (SARS-CoV-2/Norway/20365/2022) was obtained from the Norwegian Institute of Public Health, Oslo, Norway. Omicron isolate identity was confirmed by full genome sequencing and assigned by Nextclade v.2.14.1 (<https://clades.nextstrain.org>)^{67,68}. Alpha Orf6 deletion virus (Alpha Δ Orf6) was achieved by mutation of the first two methionines: MIL (A27216T) and M19L (A27200T). Reverse genetics-derived viruses were generated as previously described^{69,70}. In brief, to generate the WT SARS-CoV-2 Alpha variant, a set of overlapping viral genomic complementary DNA fragments were chemically synthesized (GENEWIZ). The cDNA fragment representing the 5' terminus of the viral genome contained the

bacteriophage T7 RNA polymerase promoter and the fragment representing the 3' terminus contained the T7 RNA polymerase termination sequences. These fragments were then assembled into a full-length Alpha cDNA genome using the transformation-associated recombination (TAR) in yeast method⁶⁹. To generate the Alpha virus carrying the ATG codon changes (M1L and M19L) in its Orf6 gene (to generate Alpha Δ Orf6), the relevant cDNA fragments were chemically synthesized (ThermoFisher) and the mutant viral genome assembled using TAR in yeast as described above. We similarly generated WT BA.5, BA.5 Δ Orf6 (carrying M1L and M19L changes), and BA.5 Orf6 D61L (generated by introducing the GAT \rightarrow CTC nucleotide change found in BA.2) using TAR in yeast except that the assembled cDNA genomes were placed under the control of the human cytomegalovirus promoter and the relevant termination sequences. The assembled WT and Orf6 null mutant genomes were transfected into BHK-hACE2-N cells stably expressing the SARS-CoV-2 N and the human ACE2 gene for virus rescue⁷¹. The rescued viruses were passaged once (P1 stock) in Vero E6 cells and their full genomes sequenced using Oxford Nanopore as previously described⁷². For Alpha and BA.5 the RG-derived viruses are referred to as WT, Δ Orf6 or Orf6 D61L to differentiate them from the clinically isolated viruses used in all other experiments. All viruses were propagated by infecting Caco-2 cells in DMEM culture medium supplemented with 1% FBS and 100 U ml⁻¹ penicillin–streptomycin at 37 °C as previously described^{1,19}. Virus was collected at 72 h.p.i. and clarified by centrifugation at 2,100g for 15 min at 4 °C to remove any cellular debris. Virus stocks were aliquoted and stored at –80 °C. Virus stocks were quantified by extracting RNA from 100 μ l of supernatant with 1 μ g ml⁻¹ carrier RNA using Qiagen RNeasy clean-up RNA protocol, before measuring viral E RNA copies ml⁻¹ by RT–qPCR^{1,19}. For experiments including Omicron subvariants XBB.1 and BQ.1.1, stocks and viral replication were quantified using Nsp12 RNA copies due to accumulation of mutations in the E gene of these variants, including in the region detected by our RT–qPCR assay. Virus titres were determined by TCID₅₀ in Hela-ACE2 cells. A total of 10⁴ cells were seeded in 96-well plates in 100 μ l. The next day, seven tenfold serial dilutions of each virus stock or supernatant were prepared and 50 μ l was added to the cells in quadruplicate. Cytopathic effect (CPE) was scored at 48–72 h.p.i. TCID₅₀ ml⁻¹ was calculated using the Reed and Muench method, and an Excel spreadsheet created by B. D. Lindenbach was used for calculating TCID₅₀ ml⁻¹ values⁷³.

To generate SARS-CoV-2 lineage frequency plots for BA.1 (B.1.1.529.1), BA.2 (B.1.1.529.2), BA.4 (B.1.1.529.4), BA.5 (B.1.1.529.5), BA.2.75 (B.1.1.529.2.75), BQ.1.1 (B.1.1.529.5.3.1.1.1.1.1), XBB.1 and XBB.1.5 (Fig. 4a and Extended Data Fig. 6a), the number of samples sequenced per week worldwide over all time was extracted for each variant on 5 August 2023 from CoV-Spectrum (cov-spectrum.org)⁷⁴ using genomic data from the Global Initiative on Sharing All Influenza Data (GISAID)⁷⁵.

Virus culture and infection

For infections, inoculum was calculated using E copies per cell quantified by RT–qPCR. Cells were inoculated with indicated variants for 2 h at 37 °C, subsequently washed with phosphate-buffered saline (PBS), and fresh DMEM culture medium supplemented with 1% FBS and 100 U ml⁻¹ penicillin–streptomycin was added. At the indicated timepoints, cells were collected for analysis. For primary HAE infections, virus was added to the apical side for 2–3 h at 37 °C. Supernatant was then removed, and cells were washed twice with PBS. All liquid was removed from the apical side, and basal medium was replaced with fresh Pneumacult ALI medium for the duration of the experiment. Virus release was measured at the indicated timepoints by extracting viral RNA from apical PBS washes. For poly(I:C) (Sigma) stimulations, cells were transfected with poly(I:C) using Lipofectamine2000 (InvitroGen) in Opti-Mem (Thermo) for the indicated times. For IFN-sensitivity assays, cells were pre-treated with indicated concentrations or recombinant human IFN β (Peprotech) for 18 h before

infection. Cytokines were maintained throughout the experiment. For inhibition assays, cells were pre-treated with 5 μ M ruxolitinib (Cambridge Bioscience), 25 μ M camostat (Apexbio), 25 μ M E64d (Focus Biomolecules) or dimethyl sulfoxide control for 2–3 h before SARS-CoV-2 infection. Inhibitors were maintained throughout the infection.

RT–qPCR of host and viral gene expression in infected cells

Infected cells were lysed in RLT (Qiagen) supplemented with 0.1% β -mercaptoethanol (Sigma). RNA extractions were performed according to the manufacturer's instructions using RNeasy Micro Kits (Qiagen) including on-column DNase I treatment (Qiagen). cDNA was synthesized using SuperScript IV (Thermo) with random hexamer primers (Thermo). RT–qPCR was performed using Fast SYBR Green Master Mix (Thermo) for host gene expression and sgRNA expression or TaqMan Master mix (Thermo Fisher Scientific) for viral RNA quantification, and reactions were performed on the QuantStudio 5 Real-Time PCR systems (Thermo Fisher Scientific). Viral E RNA copies were determined as described previously^{1,19}. Viral sgRNAs were detected using the same forward primer against the leader sequence paired with a sgRNA specific reverse primer^{1,76,77}. Using the 2^{- $\Delta\Delta$ Ct} method, sgRNA levels were normalized to *GAPDH* to account for differences in RNA loading and then normalized to the level of Orf1a gRNA quantified in the same way for each variant to account for differences in the level of infection. Host gene expression was determined using the 2^{- $\Delta\Delta$ Ct} method and normalized to *GAPDH* expression. The following probes and primers were used:

GAPDH forward: 5'-ACATCGCTCAGACACCATG-3', reverse: 5'-TGT AGTTGAGGTCAATGAAGGG-3'; *IFNB* forward: 5'-GCTTGGATTC CTACAAAGAAGCA-3', reverse: 5'-ATAGATGGTCAATGCGCGCTC-3'; *CXCL10* forward: 5'-TGGCATTCAAGGAGTACCTC-3', reverse: 5'-TT GTAGCAATGATCTCAACACG-3'; *IFIT1* forward: 5'-CCTCCT TGGGTTCTGTACA-3', reverse: 5'-GGCTGATATCTGGGTGCCTA-3'; *IFIT2* forward: 5'-CAGCTGAGAATTGCACTGCAA-3', reverse: 5'-CGTAGGCTG CTCTCCAAGGA-3'; *MX1* forward: 5'-ATCTGGGATTTTGGGGCTT-3', reverse: 5'-CCGCTTGTGCTGGTGTGCG-3'; *MX2* forward: 5'-CA GCCACCACCAGGAAAC-3', reverse: 5'-TTCTGCTCGTACTGGCTGTACAG-3'; *RSAD2* forward: 5'-CTGTCCGCTGGAAAGTG-3', reverse: 5'-GCT TCTTCTACACCAACATCC-3'; *DDX58* forward: 5'-CTGGACC CTACCTACATCCTG-3', reverse: 5'-GGCATCCAAAAAGCCACGG-3'. SARS-CoV-2 E Sarbeco forward: 5'-CGTTAATAGTTAATAGCGTA CTTCTTTTTC-3'; SARS-CoV-2 E Sarbeco Probe: 5'-FAM-ACACTAGCC ATCCTTACTGCGCTTCG-TAMRA-3'; SARS-CoV-2 E Sarbeco reverse: 5'-ATATTGCAGCAGTACGCACACA-3'; SARS-CoV-2 Nsp12 forward: 5'-GAGTGAATGGTCATGTGTGG-3'; SARS-CoV-2 Nsp12 reverse: 5'-CATTGGCCGTGACAGCTTGAC-3'; SARS-CoV-2 Nsp12 Probe: 5'-CTCATCAGGAGATGCCACAACCTGCTTATGCTAATAG-3'; 5' Leader forward: 5'-ACCAACCAACTTTTCGATCTCTTGT-3'; Orf1a reverse: 5'-CCTCCACGGAGTCTCCAAAG-3'; Orf6 reverse: GAGGTTTATGAT-GTAATCAAGATTC; N reverse: 5'-CCAGTTGAATCTGAGGGTCCAC-3'; Orf3a reverse: 5'-GCAGTAGCGGAACAAAAT-3'; S reverse: 5'-GTCAGGGTAATAAACACCACGTG-3'.

Flow cytometry

Adherent cells were trypsinized and fixed in 4% formaldehyde before intracellular staining for SARS-CoV-2 nucleocapsid (N) protein. For N detection, cells were permeabilized for 15 min with Intracellular Staining Perm Wash Buffer (BioLegend) and subsequently incubated with 1 μ g ml⁻¹ CR3009 SARS-CoV-2 cross-reactive antibody (a gift from Laura McCoy) for 30 min at room temperature. Primary antibodies were detected by incubation with secondary AlexaFluor 488-Donkey-anti-Human IgG (Jackson Labs). All samples were acquired on a BD Fortessa X20 or LSR II using BD FACSDiva software. Data were analysed using FlowJo v10.6.2 (Tree Star). Gating strategy is shown in Extended Data Fig. 7.

Cytokine secretion

Secreted mediators were detected in cell culture supernatants by ELISA. IFN β , IFN λ 1/IFN λ 3 and CXCL10 were measured using Human IFN- β Quantikine ELISA Kit, Human IL-29/IL-28B (IFN λ 1/IFN λ 3) DuoSet ELISA or Human CXCL10/IP-10 DuoSet ELISA reagents (Bio-Techne R&D Systems) according to the manufacturer's instructions.

Western blotting

For detection of N, Orf6, Orf9b, spike and β -actin expression, whole-cell protein lysates were extracted with RIPA buffer, and then separated by sodium dodecyl sulfate–polyacrylamide gel electrophoresis, transferred onto nitrocellulose and blocked in PBS with 0.05% Tween 20 and 5% skimmed milk. Membranes were probed with rabbit-anti-SARS spike (Invitrogen, PA1-411-1165, 1:1,000), mouse-anti-SARS-CoV-2 spike (GeneTex, IA9, 1:1,000), rabbit-anti-Orf6 (Abnova, PAB31757, 1:1,000), rabbit-anti-Orf9b (ProSci, 9191, 1:1,000), CR3009 SARS-CoV cross-reactive human-anti-N antibody (a gift from Laura McCoy, UCL, 1:1,000), rabbit-anti-phospho-STAT1 (Ser727; Cell Signaling, cat. no. 9177, 1:1,000), rabbit-anti-phospho-STAT1 (Tyr701; Cell Signaling, cat. no. 9167, clone 58D6, 1:1,000), rabbit-anti-STAT1 (Cell Signaling, cat. no. 9172, 1:1,000), rabbit-anti-IRF3 (Cell Signaling, cat. no. 4302, 1:1,000), rabbit-anti-phospho-IRF3 (Cell Signaling, cat. no. 29047, clone D6O1M, 1:1,000) and rabbit-anti- β -actin (A2066, Sigma, 1:2,500), followed by IRDye 800CW or 680RD secondary antibodies (Abcam, goat anti-rabbit, goat anti-mouse or goat anti-human, 1:10,000). Blots were imaged using an Odyssey Infrared Imager (LI-COR Biosciences) and analysed with Image Studio Lite software. Quantifications were performed to loading controls run on the same membrane as the protein of interest. For virion blots, live virus normalized by equal total E copies was purified across a 25% sucrose cushion and concentrated by centrifugation (2 h 16,500g, 4 °C).

Immunofluorescence staining and image analysis

Infected cells were fixed using 4% paraformaldehyde/formaldehyde for 1 h at room temperature and subsequently washed with PBS. A blocking step was carried out for 35 h at room temperature with 10% goat serum/1% bovine serum albumin/0.001 Triton X-100 in PBS. Double-stranded RNA (dsRNA) and nucleocapsid detection were performed by primary incubation with rabbit-anti-IRF3 antibody (sc-33641, Santa Cruz, 1:100), rabbit-anti-STAT1 (Cell Signaling, cat. no. 14994, clone DIK9Y, 1:100), mouse-anti-dsRNA (MABE1134, Millipore, 1:100) and CR3009 SARS-CoV cross-reactive human-anti-N antibodies (1:1,000) for 18 h and washed thoroughly in PBS. Primary antibodies detection occurred using secondary anti-rabbit-AlexaFluor-488, anti-mouse-AlexaFluor-568 and anti-human-Alexa647 conjugates (Jackson ImmunoResearch, 1:500) for 1 h. All cells were labelled with Hoechst33342 (H3570, Thermo Fisher, 1:5,000). Images were acquired using the WiScan Hermes 7-Colour High-Content Imaging System (IDEA Bio-Medical) at magnification 10 \times /0.4 numerical aperture. Four-channel automated acquisition was carried out sequentially. Images were acquired across a well area density resulting in 31 fields of view per well and ~20,000 cells. Images were pre-processed by applying a batch rolling ball background correction in FIJI ImageJ software package⁷⁸ before quantification. IRF3 and STAT1 translocation analysis was carried out using the Athena Image analysis software (IDEA Bio-Medical) and data post-processed in Python. For dsRNA, infected cell populations were determined by thresholding of populations with more than two segmented dsRNA punctae. For transcription factor translocation analysis, infected populations were determined by presence of segmented nucleocapsid signal within the cell.

Image pre-processing was carried out using a custom macro applying a 30-pixel rolling ball background subtraction to all channels. Single-cell automated image analysis was carried out using the Athena image analysis software 'Nuclear Translocation Assay'⁷⁹ (IDEA-BioMedical). Within the Athena software, nuclei were segmented using the Hoechst33342

channel, and dsRNA/N channels were segmented as 'cytoplasmic granules' thresholded according to the mock infected population to identify infected cells. The cellular periphery was segmented by STAT1/IRF3 channels. The raw single-cell data were processed in a Python 3 script using the Pandas Data analysis library (<https://pandas.pydata.org>). In short, the mean nuclear:cytoplasmic ratio was calculated from the raw data. The data were 'top and tail' filtered, dropping the lowest and highest percentile for the following metrics: cell area, nuclear area, mean nuclear intensity and mean cytoplasmic intensity (STAT1/IRF3). The data were filtered into 'infected cells' by the presence of segmented cytoplasmic granules (dsRNA/N) or 'bystander cells' for their absence. The filtered data were then randomly sampled in the same Python environment. ImageJ macro and Python post-processing pipelines are available upon request.

Statistical analysis

Statistical analysis was performed using GraphPad Prism9, and details of statistical tests used are indicated. Data distribution was assumed to be normal unless stated differently, but this was not formally tested. No statistical methods were used to pre-determine sample sizes, but our sample sizes are similar to those reported in previous publications^{1,19}. Data collection and analysis were not performed blind to the conditions of the experiments.

Reporting summary

Further information on research design is available in the Nature Portfolio Reporting Summary linked to this article.

Data availability

All data generated or analysed during this study are included in this paper (and its [Supplementary Information](#) files). No datapoints were excluded. Representative microscopy images can be accessed through FigShare via <https://doi.org/10.6084/m9.figshare.24781893.v1>⁸⁰. SARS-CoV-2 variant sequence counts were extracted from CoV-Spectrum (cov-spectrum.org)⁷⁴ using genomic data from GISAID⁷⁵. Source data are provided with this paper.

Code availability

The ImageJ macro and Python post-processing pipelines are available at https://github.com/MattVXWhelan/Reuschl_et_al_Nature_Micro.

References

1. Thorne, L. G. et al. Evolution of enhanced innate immune evasion by SARS-CoV-2. *Nature* **602**, 487–495 (2022).
2. Bouhaddou, M. et al. SARS-CoV-2 variants evolve convergent strategies to remodel the host response. *Cell* **186**, 4597–4614. e26 (2023).
3. Hansen, C. H. et al. Risk of reinfection, vaccine protection, and severity of infection with the BA.5 omicron subvariant: a nation-wide population-based study in Denmark. *Lancet Infect. Dis.* **23**, 167–176 (2023).
4. Wolter, N. et al. Early assessment of the clinical severity of the SARS-CoV-2 omicron variant in South Africa: a data linkage study. *Lancet* **399**, 437–446 (2022).
5. Viana, R. et al. Rapid epidemic expansion of the SARS-CoV-2 Omicron variant in southern Africa. *Nature* **603**, 679–686 (2022).
6. Pulliam, J. R. C. et al. Increased risk of SARS-CoV-2 reinfection associated with emergence of Omicron in South Africa. *Science* **376**, eabn4947 (2022).
7. Tegally, H. et al. Emergence of SARS-CoV-2 Omicron lineages BA.4 and BA.5 in South Africa. *Nat. Med.* **28**, 1785–1790 (2022).
8. Cao, Y. et al. BA.2.12.1, BA.4 and BA.5 escape antibodies elicited by Omicron infection. *Nature* **608**, 593–602 (2022).
9. Gruell, H. et al. SARS-CoV-2 Omicron sublineages exhibit distinct antibody escape patterns. *Cell Host Microbe* **30**, 1231–1241.e6 (2022).

10. Wang, Q. et al. Antibody evasion by SARS-CoV-2 Omicron subvariants BA.2.12.1, BA.4 and BA.5. *Nature* **608**, 603–608 (2022).
11. Tuekprakhon, A. et al. Antibody escape of SARS-CoV-2 Omicron BA.4 and BA.5 from vaccine and BA.1 serum. *Cell* **185**, 2422–2433.e13 (2022).
12. Willett, B. J. et al. Distinct antigenic properties of the SARS-CoV-2 Omicron lineages BA.4 and BA.5. Preprint at *bioRxiv* <https://doi.org/10.1101/2022.05.25.493397> (2022).
13. Kimura, I. et al. Virological characteristics of the SARS-CoV-2 Omicron BA.2 subvariants, including BA.4 and BA.5. *Cell* **185**, 3992–4007.e16 (2022).
14. Khan, K. et al. Omicron BA.4/BA.5 escape neutralizing immunity elicited by BA.1 infection. *Nat. Commun.* **13**, 4686 (2022).
15. Steel, K., Fordham, E. & Bracher, M. Coronavirus (COVID-19) Infection Survey, UK. Office for National Statistics <https://www.ons.gov.uk/peoplepopulationandcommunity/healthandsocialcare/conditionsanddiseases/bulletins/coronaviruscovid19infectionsurvey/pilot/8july2022> (2022).
16. Hachmann, N. P. et al. Neutralization escape by SARS-CoV-2 Omicron subvariants BA.2.12.1, BA.4, and BA.5. *N. Engl. J. Med.* **387**, 86–88 (2022).
17. Chen, D.-Y. et al. Spike and nsp6 are key determinants of SARS-CoV-2 Omicron BA.1 attenuation. *Nature* **615**, 143–150 (2023).
18. Hossain, A., Akter, S., Rashid, A. A., Khair, S. & Alam, A. S. M. R. U. Unique mutations in SARS-CoV-2 Omicron subvariants' non-spike proteins: potential impacts on viral pathogenesis and host immune evasion. *Microb. Pathog.* **170**, 105699 (2022).
19. Thorne, L. G. et al. SARS-CoV-2 sensing by RIG-I and MDA5 links epithelial infection to macrophage inflammation. *EMBO J.* **40**, e107826 (2021).
20. Meng, B. et al. Altered TMPRSS2 usage by SARS-CoV-2 Omicron impacts infectivity and fusogenicity. *Nature* **603**, 706–714 (2022).
21. Peacock, T. P. et al. The altered entry pathway and antigenic distance of the SARS-CoV-2 Omicron variant map to separate domains of spike protein. Preprint at *bioRxiv* <https://doi.org/10.1101/2021.12.31.474653> (2022).
22. Willett, B. J. et al. SARS-CoV-2 Omicron is an immune escape variant with an altered cell entry pathway. *Nat. Microbiol.* **7**, 1161–1179 (2022).
23. Mesner, D. et al. SARS-CoV-2 evolution influences GBP and IFITM sensitivity. *Proc. Natl Acad. Sci. USA* **120**, e2212577120 (2023).
24. Hoffmann, M., Kleine-Weber, H. & Pöhlmann, S. A multibasic cleavage site in the spike protein of SARS-CoV-2 is essential for infection of human lung cells. *Mol. Cell* **78**, 779–784.e5 (2020).
25. Hoffmann, M. et al. SARS-CoV-2 cell entry depends on ACE2 and TMPRSS2 and is blocked by a clinically proven protease inhibitor. *Cell* **181**, 271–280.e8 (2020).
26. Stanifer, M. L. et al. Critical role of type III interferon in controlling SARS-CoV-2 infection in human intestinal epithelial cells. *Cell Rep.* **32**, 107863 (2020).
27. V'kovski, P. et al. Disparate temperature-dependent virus–host dynamics for SARS-CoV-2 and SARS-CoV in the human respiratory epithelium. *PLoS Biol.* **19**, e3001158 (2021).
28. Foxman, E. F., Storer, J. A., Vanaja, K., Levchenko, A. & Iwasaki, A. Two interferon-independent double-stranded RNA-induced host defense strategies suppress the common cold virus at warm temperature. *Proc. Natl Acad. Sci. USA* **113**, 8496–8501 (2016).
29. Foxman, E. F. et al. Temperature-dependent innate defense against the common cold virus limits viral replication at warm temperature in mouse airway cells. *Proc. Natl Acad. Sci. USA* **112**, 827–832 (2015).
30. Huang, D. et al. Cold exposure impairs extracellular vesicle swarm-mediated nasal antiviral immunity. *J. Allergy Clin. Immunol.* **151**, 509–525.e8 (2023).
31. Khosravi, M. et al. A distinct difference between air and mucosal temperatures in human respiratory tract. *Front. Med.* **8**, 650637 (2021).
32. Kehrler, T. et al. Impact of SARS-CoV-2 ORF6 and its variant polymorphisms on host responses and viral pathogenesis. *Cell Host Microbe* **31**, 1668–1684 (2023).
33. Sadzak, I. et al. Recruitment of Stat1 to chromatin is required for interferon-induced serine phosphorylation of Stat1 transactivation domain. *Proc. Natl Acad. Sci. USA* **105**, 8944–8949 (2008).
34. Kimura, I., Konno, Y., Sauter, D., Nakagawa, S. & Sato, K. Sarbecovirus ORF6 proteins hamper the induction of interferon signaling by blocking mRNA nuclear export. *Cell Rep.* **34**, 108916 (2021).
35. Miorin, L. et al. SARS-CoV-2 Orf6 hijacks Nup98 to block STAT nuclear import and antagonize interferon signaling. *Proc. Natl Acad. Sci. USA* **117**, 28344–28354 (2020).
36. Lei, X. et al. Activation and evasion of type I interferon responses by SARS-CoV-2. *Nat. Commun.* **11**, 3810 (2020).
37. Kimura, I. et al. Sarbecovirus ORF6 proteins hamper induction of interferon signaling. *Cell Rep.* **34**, 108916 (2021).
38. Addetia, A. et al. SARS-CoV-2 ORF6 disrupts bidirectional nucleocytoplasmic transport through interactions with Rae1 and Nup98. *mBio* **12**, e00065–21 (2021).
39. Gori Savellini, G., Anichini, G. & Cusi, M. G. SARS-CoV-2 omicron sub-lineages differentially modulate interferon response in human lung epithelial cells. *Virus Res.* **332**, 199134 (2023).
40. Saito, A. et al. Virological characteristics of the SARS-CoV-2 Omicron BA.2.75 variant. *Cell Host Microbe* **30**, 1540–1555.e15 (2022).
41. Tamura, T. et al. Virological characteristics of the SARS-CoV-2 XBB variant derived from recombination of two Omicron subvariants. *Nat. Commun.* **14**, 2800 (2023).
42. Uriu, K. et al. Enhanced transmissibility, infectivity, and immune resistance of the SARS-CoV-2 omicron XBB.1.5 variant. *Lancet Infect. Dis.* **23**, 280–281 (2023).
43. Ito, J. et al. Convergent evolution of SARS-CoV-2 Omicron subvariants leading to the emergence of BQ.1.1 variant. *Nat. Commun.* **14**, 2671 (2023).
44. Cheemarla, N. R. et al. Dynamic innate immune response determines susceptibility to SARS-CoV-2 infection and early replication kinetics. *J. Exp. Med.* **218**, e20210583 (2021).
45. Loske, J. et al. Pre-activated antiviral innate immunity in the upper airways controls early SARS-CoV-2 infection in children. *Nat. Biotechnol.* **40**, 319–324 (2022).
46. Park, A., & Iwasaki, A. Type I and type III interferons—induction, signaling, evasion, and application to combat COVID-19. *Cell Host Microbe* **27**, 870–878 (2020).
47. Zhang, Q. et al. Inborn errors of type I IFN immunity in patients with life-threatening COVID-19. *Science* **370**, eabd4570 (2020).
48. Bastard, P. et al. Autoantibodies against type I IFNs in patients with life-threatening COVID-19. *Science* **370**, eabd4585 (2020).
49. Pairo-Castineira, E. et al. Genetic mechanisms of critical illness in COVID-19. *Nature* **591**, 92–98 (2021).
50. Zhang, Q. & Bastard, P., COVID Human Genetic Effort, Cobat, A. & Casanova, J.-L. Human genetic and immunological determinants of critical COVID-19 pneumonia. *Nature* **603**, 587–598 (2022).
51. Wickenhagen, A. et al. A prenylated dsRNA sensor protects against severe COVID-19. *Science* **374**, eabj3624 (2021).
52. Selvaraj, V. et al. Baricitinib in hospitalised patients with COVID-19: a meta-analysis of randomised controlled trials. *eClinicalMedicine* **49**, 101489 (2022).
53. Sandler, N. G. et al. Type I interferon responses in rhesus macaques prevent SIV infection and slow disease progression. *Nature* **511**, 601–605 (2014).

54. Killingley, B. et al. Safety, tolerability and viral kinetics during SARS-CoV-2 human challenge in young adults. *Nat. Med.* **28**, 1031–1041 (2022).
55. Rosenheim, J. et al. SARS-CoV-2 human challenge reveals single-gene blood transcriptional biomarkers that discriminate early and late phases of acute respiratory viral infections. Preprint at *medRxiv* <https://doi.org/10.1101/2023.06.01.23290819> (2023).
56. Brant, A. C., Tian, W., Majerciak, V., Yang, W. & Zheng, Z.-M. SARS-CoV-2: from its discovery to genome structure, transcription, and replication. *Cell Biosci.* **11**, 136 (2021).
57. Pagani, I., Ghezzi, S., Alberti, S., Poli, G. & Vicenzi, E. Origin and evolution of SARS-CoV-2. *Eur. Phys. J.* **138**, 157 (2023).
58. Silvas, J. A. et al. Contribution of SARS-CoV-2 accessory proteins to viral pathogenicity in K18 human ACE2 transgenic mice. *J. Virol.* <https://doi.org/10.1128/jvi.00402-21> (2021).
59. Chin, A. W. H., Lai, A. M. Y., Peiris, M. & Man Poon, L. L. Increased stability of SARS-CoV-2 omicron variant over ancestral strain. *Emerg. Infect. Dis.* **28**, 1515–1517 (2022).
60. Hirose, R. et al. Differences in environmental stability among SARS-CoV-2 variants of concern: both omicron BA.1 and BA.2 have higher stability. *Clin. Microbiol. Infect.* **28**, 1486–1491 (2022).
61. SARS-ANI VIS. *Complexity Science Hub* <https://vis.csh.ac.at/sars-ani/> (2022).
62. Lee, I. T. et al. ACE2 localizes to the respiratory cilia and is not increased by ACE inhibitors or ARBs. *Nat. Commun.* **11**, 1–14 (2020).
63. Pinto, R. M. et al. BTN3A3 evasion promotes the zoonotic potential of influenza A viruses. *Nature* **619**, 338–347 (2023).
64. Riegger, D. et al. The nucleoprotein of newly emerged H7N9 influenza A virus harbors a unique motif conferring resistance to antiviral human MxA. *J. Virol.* <https://doi.org/10.1128/jvi.02406-14> (2014).
65. Zuliani-Alvarez, L. et al. Evasion of cGAS and TRIM5 defines pandemic HIV. *Nat. Microbiol.* **7**, 1762–1776 (2022).
66. Rogers, T. F. et al. Isolation of potent SARS-CoV-2 neutralizing antibodies and protection from disease in a small animal model. *Science* **369**, 956–963 (2020).
67. Hadfield, J. et al. Nextstrain: real-time tracking of pathogen evolution. *Bioinformatics* **34**, 4121–4123 (2018).
68. Aksamentov, I., Roemer, C., Hodcroft, E. & Neher, R. Nextclade: clade assignment, mutation calling and quality control for viral genomes. *J. Open Source Softw.* **6**, 3773 (2021).
69. Zhou, J. et al. Mutations that adapt SARS-CoV-2 to mink or ferret do not increase fitness in the human airway. *Cell Rep.* **38**, 110344 (2022).
70. Thi Nhu Thao, T. et al. Rapid reconstruction of SARS-CoV-2 using a synthetic genomics platform. *Nature* **582**, 561–565 (2020).
71. Rihn, S. J. et al. A plasmid DNA-launched SARS-CoV-2 reverse genetics system and coronavirus toolkit for COVID-19 research. *PLoS Biol.* **19**, e3001091 (2021).
72. da Silva Filipe, A. et al. Genomic epidemiology reveals multiple introductions of SARS-CoV-2 from mainland Europe into Scotland. *Nat. Microbiol.* **6**, 112–122 (2021).
73. Lindenbach, B. D. Measuring HCV infectivity produced in cell culture and in vivo. *Hepat. C* **510**, 329–336 (2009).
74. Chen, C. et al. CoV-Spectrum: analysis of globally shared SARS-CoV-2 data to identify and characterize new variants. *Bioinformatics* **38**, 1735–1737 (2022).
75. Elbe, S. & Buckland-Merrett, G. Data, disease and diplomacy: GISAIID's innovative contribution to global health. *Glob. Chall.* **1**, 33–46 (2017).
76. Parker, M. D. et al. Altered subgenomic RNA abundance provides unique insight into SARS-CoV-2 B.1.1.7/Alpha variant infections. *Commun. Biol.* **5**, 666 (2022).
77. Meredith, L. W. et al. Rapid implementation of SARS-CoV-2 sequencing to investigate cases of health-care associated COVID-19: a prospective genomic surveillance study. *Lancet Infect. Dis.* **20**, 1263–1271 (2020).
78. Schindelin, J. et al. Fiji: an open-source platform for biological-image analysis. *Nat. Methods* **9**, 676–682 (2012).
79. Cytoplasm to nuclear translocation assay. *IDEA Bio-Medical* <https://idea-bio.com/all-applications/application-nuclear-translocation/>
80. Reuschl, A.-K. Evolution of enhanced innate immune suppression by SARS-CoV-2 Omicron subvariants. *figshare* <https://doi.org/10.6084/m9.figshare.24781893.v1> (2023).

Acknowledgements

This work was funded by Wellcome Investigator Awards 223065 to C.J. and 220863 to G.J.T. G.J.T. and C.J. were also funded by MRC/UKRI G2P-UK and G2P2 National Virology consortia (MR/W005611/1 and MR/Y004205/1) and the UCL COVID-19 fund. R.R. is supported by a Marie Skłodowska-Curie Individual Fellowships no. 896014. P.B. received funding from the European Research Council (ERC-Stg no. 639429), the Rosetrees Trust (M362-F1; M553), the NIHR GOSH BRC and the CF Trust (SRC006; SRC020). M.V.X.W. is supported by a Wellcome Trust Early Career Award Fellowship (227004/Z/23/Z), the NIHR Biomedical Research Centre at UCLH and IDEA Bio-Medical. The work at the CVR was funded by G2P-UK National Virology Consortium funded by the MRC (MR/W005611/1) and MRC grants (MC_UU12014/2 and MC_UU_00034/9) and the Wellcome Trust (206369/Z/17/Z). We are grateful to W. Barclay (Imperial College London, United Kingdom), A. Sigal and K. Khan (AHRI, South Africa) and the Norwegian Institute of Public Health for provision of virus isolates and D. Bailey (Pirbright Institute, United Kingdom), L. McCoy (University College London, United Kingdom) and J. Voss (Scripps Institute, United States) for reagents. We thank J. Evans (University College London, United Kingdom) for their assistance at the UCL Rayne flow cytometry core facility.

Author contributions

A.-K.R., L.G.T., G.J.T. and C.J. conceptualized the study. A.-K.R., L.G.T., V.M.C., W.F., G.D.L., G.J.T. and C.J. designed experiments. A.-K.R., L.G.T., M.X.V.W., D.M., G.D., N.B., V.M.C., W.F. and G.D.L. performed experiments. A.-K.R., L.G.T., M.X.V.W., G.J.T. and C.J. analysed data. A.-K.R., R.R., W.F., G.D.L., V.M.C., J.L.E.T., P.B., M.P. and A.H.P. generated and provided reagents. A.-K.R., L.G.T., D.M., A.H.P., M.P., G.J.T. and C.J. prepared and edited the paper. P.B., M.P., A.H.P., G.J.T. and C.J. coordinated and supervised the study.

Competing interests

The authors declare no competing interests.

Additional information

Extended data is available for this paper at <https://doi.org/10.1038/s41564-023-01588-4>.

Supplementary information The online version contains supplementary material available at <https://doi.org/10.1038/s41564-023-01588-4>.

Correspondence and requests for materials should be addressed to Ann-Kathrin Reuschl, Clare Jolly or Greg J. Towers.

Peer review information *Nature Microbiology* thanks Xing-Yi Ge, Natalia Sampaio, Xiangxi Wang and the other, anonymous, reviewer(s) for their contribution to the peer review of this work.

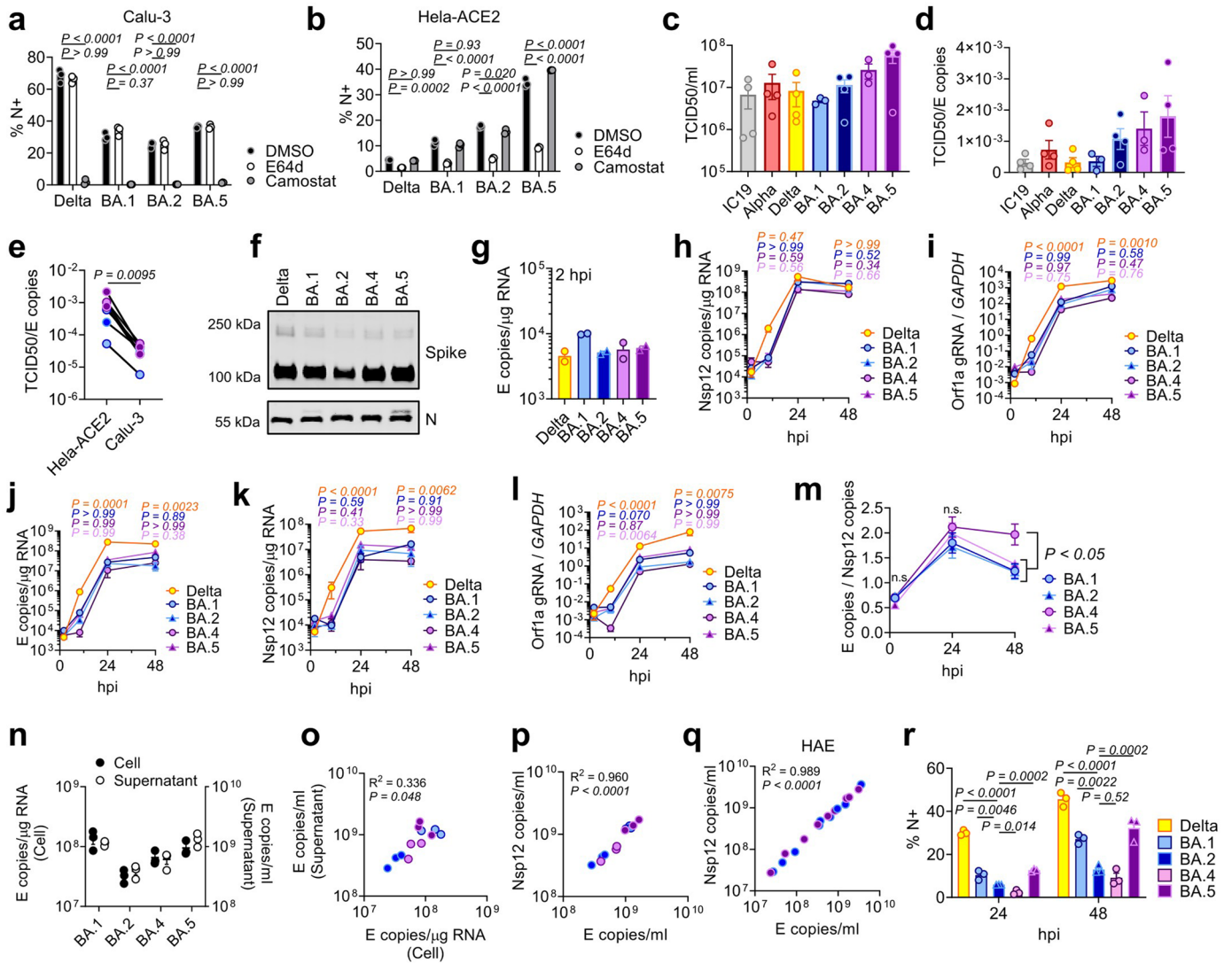
Reprints and permissions information is available at www.nature.com/reprints.

Publisher's note Springer Nature remains neutral with regard to jurisdictional claims in published maps and institutional affiliations.

Open Access This article is licensed under a Creative Commons Attribution 4.0 International License, which permits use, sharing, adaptation, distribution and reproduction in any medium or format, as long as you give appropriate credit to the original author(s) and the source, provide a link to the Creative Commons license, and indicate if changes were made. The images or other third party material in this

article are included in the article's Creative Commons license, unless indicated otherwise in a credit line to the material. If material is not included in the article's Creative Commons license and your intended use is not permitted by statutory regulation or exceeds the permitted use, you will need to obtain permission directly from the copyright holder. To view a copy of this license, visit <http://creativecommons.org/licenses/by/4.0/>.

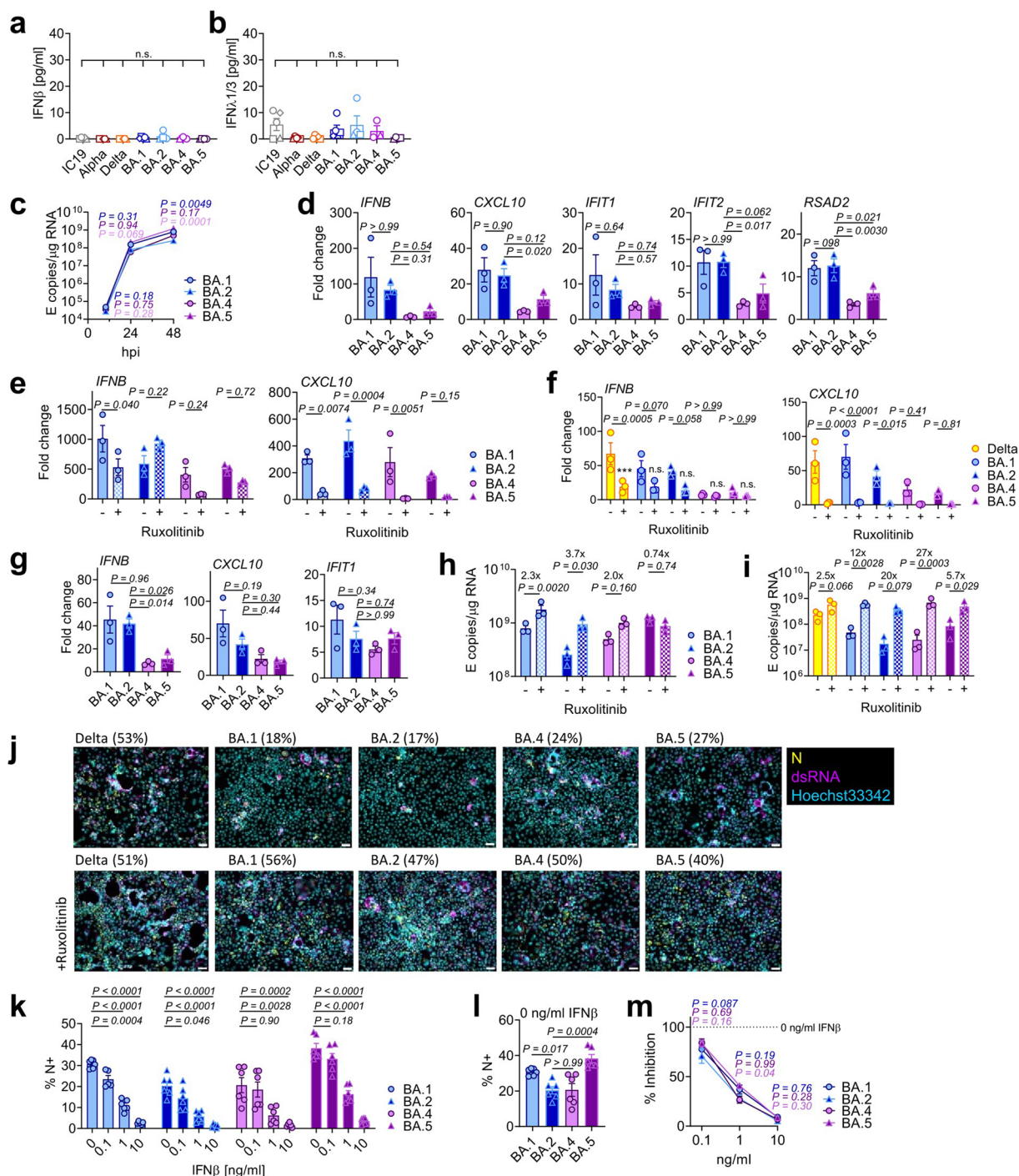
© The Author(s) 2024



Extended Data Fig. 1 | Replication measurements of SARS-CoV-2 variants.

(a) Calu-3 and (b) HeLa-ACE2 were infected with 1000 E copies/cell in the presence of DMSO (-), 25 μM E64d or 25 μM Camostat. Infection levels at 24 hpi by nucleocapsid expression, one of two independent experiments shown. (c) Quantification of viral stocks used in Figs. 1 and 2 by TCID₅₀/ml on HeLa-ACE2. Each symbol indicates an independent virus stock. (d) Ratio of TCID₅₀/ml over E copies/ml for virus stocks from (d). (e) TCID₅₀/ml over E copies/ml of virus stocks measured on HeLa-ACE2 or Calu-3 cells. (f) Western blot of purified SARS-CoV-2 virions, n = 2. (g) Calu-3 infection with 200 E copies/cell of Delta (yellow; ○), BA.1 (blue; ○), BA.2 (blue; Δ), BA.4 (purple; ○) and BA.5 (purple; Δ). Viral replication at 2 hpi. (h) Nsp12 copies/μg RNA or (i) Orf1a gRNA/GAPDH in cells from Fig. 1a. Viral replication measured by (j) E copies/μg RNA, (k) Nsp12 copies/μg RNA or (l) Orf1a gRNA/GAPDH in cells infected with 200 E copies/ml. (m) E copies/Nsp12 copies in Calu-3 cells. Nine replicates from three independent experiments shown. (n-p)

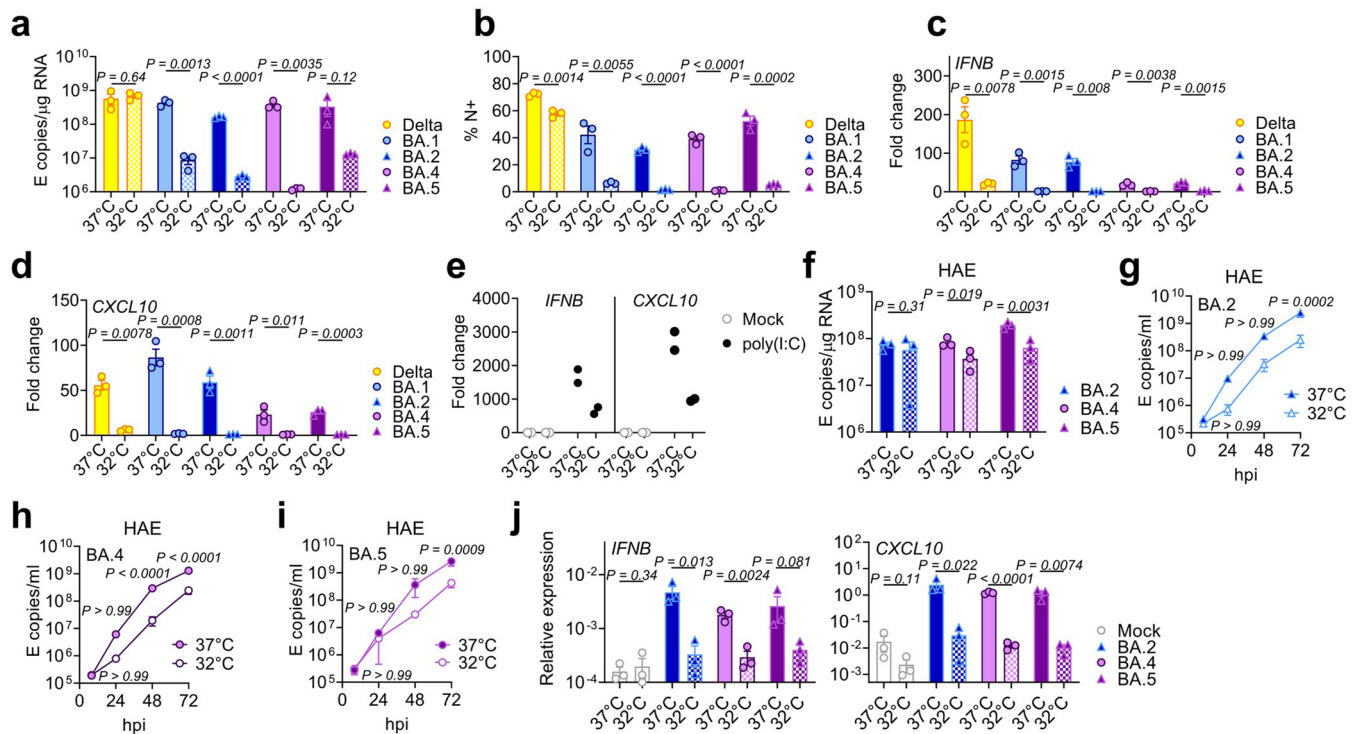
Calu-3 cells were infected with 2000 E copies/cell. (n) Intracellular replication (Cell) and viral release (Supernatant) was determined by quantification of E copies at 24 hpi. (o) Correlation graph of intracellular E copies and virus released into supernatant at 24 hpi. (p) Nsp12 and E gene copies correlation in supernatants from (n). (q) Correlation of Nsp12 and E copies in apical washes from HAEs infected with BA.2 (blue) or BA.5 (purple) (samples from Fig. 4). (r) Infections levels measured by nucleocapsid expression in cells from (j). For a, b, h-l, r, one-way ANOVA with a Dunnett post-test was used. For a, b, groups were compared to DMSO. For e, paired Student's t-Test was used. For h-m, groups were compared to BA.2 and colors indicate comparator (Delta, yellow; BA.1, blue; BA.4, purple; BA.5, pink). For m, n.s. is not significant at P > 0.05 for all comparisons. For o,p,q, simple linear regression was used. Triplicate measurements from representative experiments. Mean ± SEM or individual datapoints shown. hpi, hours post infection. gRNA, genomic RNA.



Extended Data Fig. 2 | BA.5 displays enhanced innate immune antagonism during infection of airway epithelial cells.

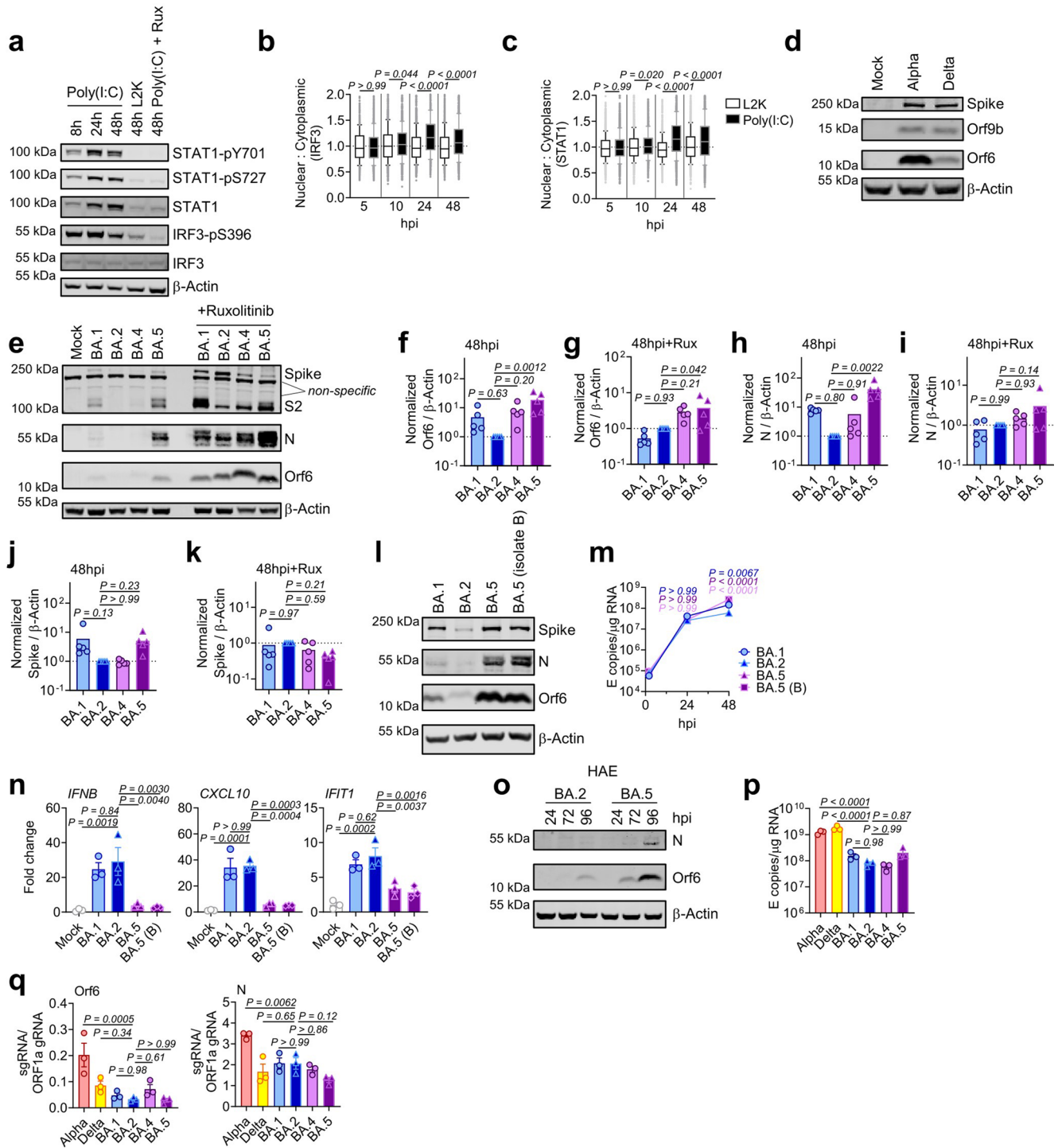
(a) IFN β and (b) IFN λ 1/3 levels detected in SARS-CoV-2 variant inoculum prepared from virus stocks prepped in Caco-2 cells. Symbols indicate independent virus stocks, 3–5 stocks are shown. (c–e) Calu-3 infection with 2000 E copies/cell of BA.1 (blue; O), BA.2 (blue; Δ), BA.4 (purple; O) and BA.5 (purple; Δ). (c) Viral replication over time. (d) IFNB, CXCL10, IFIT1, IFIT2 and RSAD2 gene expression at 24hpi. (e) Gene expression in the presence of ruxolitinib in cells from (c). (f) Gene expression in the presence of ruxolitinib in cells from Extended Data Fig. 1j at 24hpi. (g) Gene expression in infected cells at 24hpi in cells from Extended Data Fig. 1j. (h) Viral replication of indicated variants in the presence or absence of 5 μ M ruxolitinib at 48hpi in cells from (c). (i) Viral replication of indicated variants in Calu-3 cells from Extended Data Fig. 1j in the presence or absence of 5 μ M ruxolitinib at 48hpi. (j) Fluorescence microscopy of Calu-3 cells infected at 2000 E copies/cell at 48hpi in the presence or absence of 5 μ M ruxolitinib. Percentage infection quantified by

dsRNA-positive cells is indicated per condition. Nucleocapsid (N), yellow; dsRNA, magenta; Hoechst33342, cyan. Representative images from cells in Fig. 1b are shown. Scale bar, 50 μ m. (k–m) IFN β -sensitivity of indicated variants during Calu-3 cell infection at 2000 E copies/cell. (k) Infection levels measured by % N+ at 24hpi at the indicated concentrations of IFN β . (l) Infection levels in cells from (k) at 0 ng/ml IFN β . (m) Infection levels from (k) normalized to 0 ng/ml IFN β for each variant. Six measurements from two independent experiments shown. One-way ANOVA and Dunnett's post-test were used. Groups were compared as indicated or with BA.2. For a, b, comparisons were made using one-way ANOVA and Bonferroni post-test. For e, comparisons were made against 0 ng/ml IFN β for each variant. Colors in c and m indicate comparator (BA.1, blue; BA.4, purple; BA.5, pink). Fold change over mock is shown. Triplicate measurements from independent experiments are shown. Mean \pm SEM or individual datapoints are shown. hpi, hours post infection.



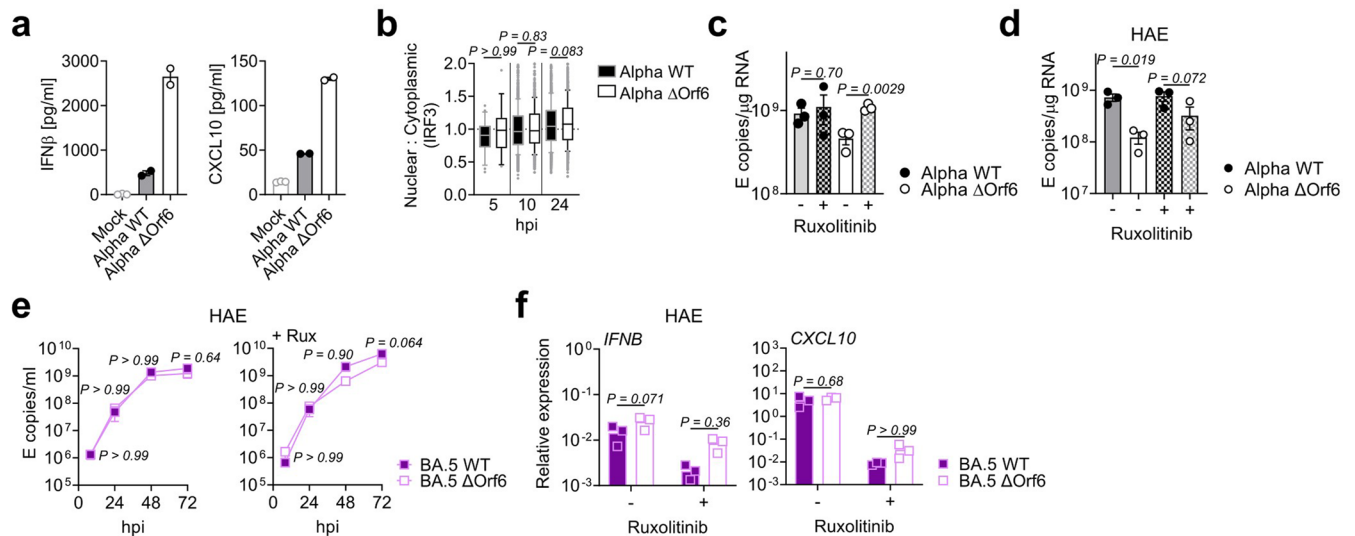
Extended Data Fig. 3 | Entry and replication characteristics of Omicron subvariant BA.5. (a–d) Calu-3 cells were infected with 2000 E copies/cell at 37 °C or 32 °C, one representative of two independent experiments shown. (a) Viral replication by RT-qPCR and (b) infection levels by flow cytometry at 24hpi. (c) *IFNB* and (d) *CXCL10* expression in cells from (a). (e) *IFNB* and *CXCL10* expression in response to poly(I:C) transfection in Calu-3 cells at 24h of stimulation, two replicates shown. (f–j) Primary bronchial human airway epithelial cells (HAEs) were infected with 1500 E copies/cell of the indicated variants at 37 °C or

32 °C. Three biological replicates shown. Viral replication was measured by (f) intracellular E copies at 72hpi and viral release of (g) BA.2, (h) BA.4 and (i) BA.5 into apical washes over time. Relative expression of (j) *IFNB* and *CXCL10* normalized to *GAPDH* in cells from (f). Fold changes are normalized to mock. Pairwise comparisons were performed using an unpaired two-tailed Student's t-Test as indicated. For g–i, two-way ANOVA with a Bonferroni post-test was used to compare temperatures at each time point. Fold change over mock is shown. Mean \pm SEM or individual datapoints are shown. hpi, hours post infection.



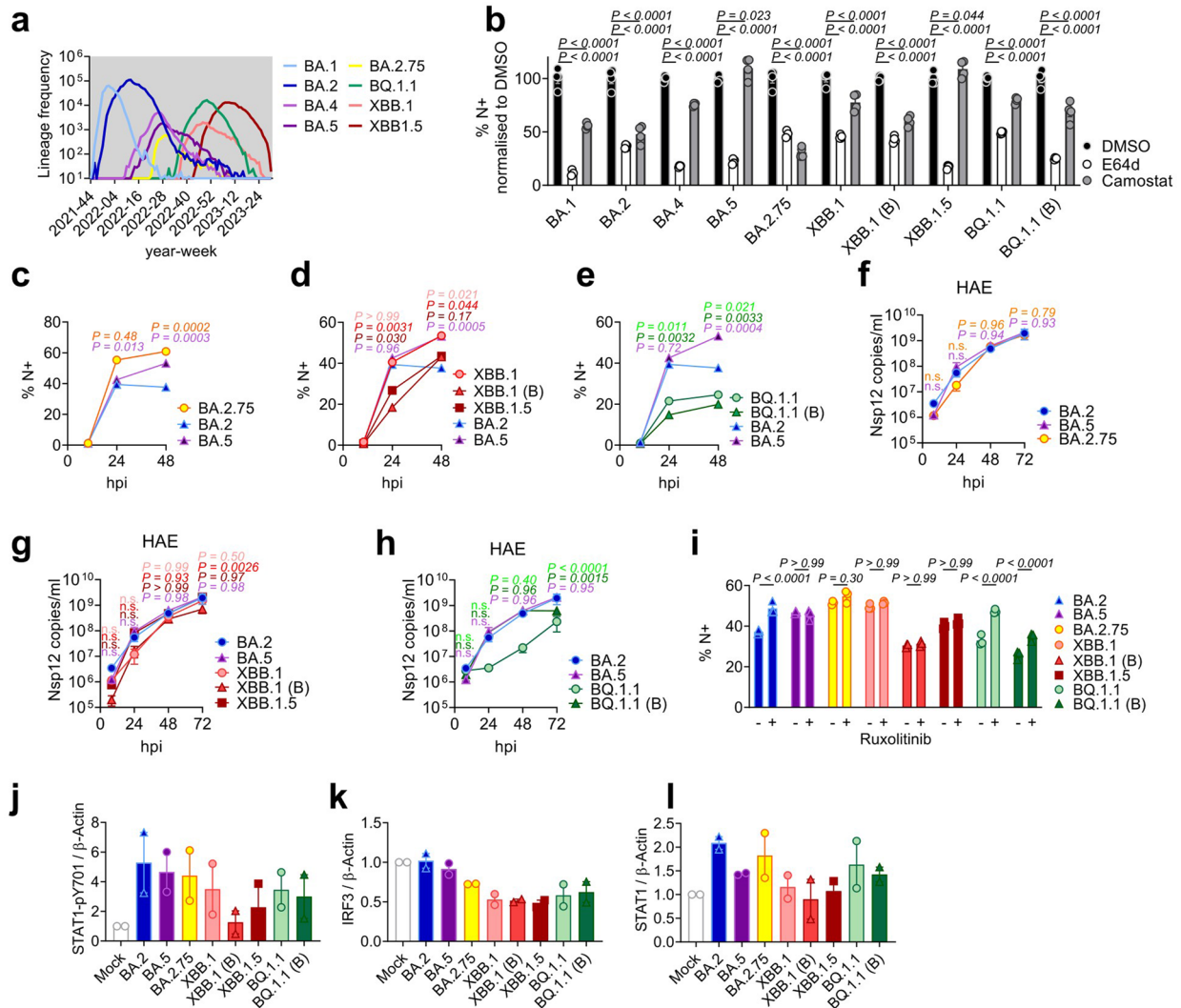
Extended Data Fig. 4 | BA.5 efficiently expresses SARS-CoV-2 innate antagonists during airway epithelial cell infection. (a) Western blot of Calu-3 cells treated with poly(I:C), vehicle control lipofectamin2000 (L2K) or 5 μM ruxolitinib (Rux) where indicated. STAT1-pY701, STAT1-pS727, total STAT1, IRF3-pS396, total IRF3, and β-actin are shown at indicated time points. (b, c) Quantification of (b) IRF3 and (c) STAT1 nuclear translocation detected by single-cell fluorescence microscopy in Calu-3 cells stimulated with poly(I:C) or L2K. Data from 1500 cells/condition are shown. (d) Western blot of Orf9b, Orf6, spike and β-actin at 24hpi in Calu-3 cells infected with the indicated variants at 2000 E copies/cell. (e) Representative western blot of infected Calu-3 cells ± 5 μM ruxolitinib. Non-specific bands detected by polyclonal anti-spike primary antibody are indicated. (f-k) Quantification of viral protein expression from five independent western blots of infected Calu-3 cells at 48hpi ± 5 μM ruxolitinib. (f, g) Orf6, (h, i) N and (j, k) spike were normalized to β-Actin over BA.2. (l) Western blot of Calu-3 cells infected with BA.1, BA.2 and two independent BA.5 isolates at

48hpi. (m, n) Calu-3 cells were infected with BA.1, BA.2 and two independent BA.5 isolates and (m) replication measured. (n) Expression of *IFNB*, *CXCL10* and *IFIT1* is shown at 24hpi in cells from (m). (o) Representative western blot of Orf6 and N expression by HAEs infected with 1500 E copies/cell of BA.2 or BA.5 over time. (p) Viral replication in Calu-3 cells by RT-qPCR at 24hpi. (q) Orf6 and N sgRNA expression in cells from (n). For b, box and whisker blots show 10–90 percentile and groups were compared at each time point as indicated using a Kruskal-Wallis test. For f-k, n, p-q, one-way ANOVA with Dunnett’s post-test was used to compare BA.2 with other variants. For m, two-way ANOVA with a Bonferroni post-test was used to compare variants with BA.2 at each time point. Colors indicate comparator (BA.1, blue BA.5, purple; BA.5 (B), pink). For f-k, m-n, p-q, replicate measurements from one of two independent experiments are shown. Fold change over mock is shown. Mean ± SEM or individual datapoints are shown. hpi, hours post infection. sgRNA, subgenomic RNA.



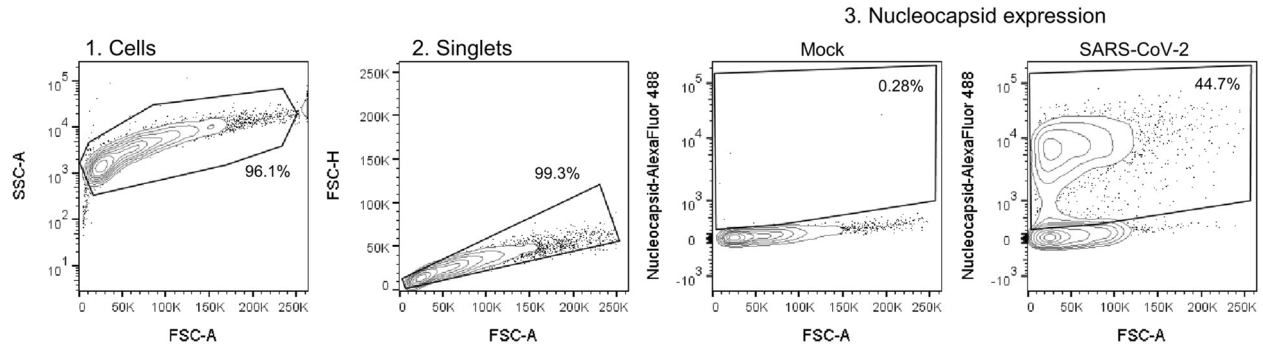
Extended Data Fig. 5 | Orf6 expression is a major determinant of enhanced innate immune antagonism by emerging VOCs. (a) IFN β and CXCL10 secretion from infected Calu-3 cells measured at 48hpi, replicate measurements from one of two independent experiments shown. (b) Quantification of IRF3 nuclear translocation in Calu-3 cells infected with Alpha WT and Alpha Δ Orf6 detected by single-cell fluorescence microscopy over time. Data from 1500 cells/condition are shown. (c) Viral replication in the presence or absence of 5 μ M ruxolitinib (Rux) at 48hpi in cells from Fig. 3c. One representative of three independent experiments shown. (d) HAEs were infected with 1500 E copies/cell of the indicated variants in the presence or absence of 5 μ M ruxolitinib. Intracellular

E copies from three biological replicates are shown. Apical washes are shown in Fig. 3f–h. (e, f) Infection of HAEs with BA.5 WT or BA.5 Δ Orf6 with 1500 E copies/cell showing (e) viral release into apical washes over time or (f) *IFN β* and *CXCL10* normalized to *GAPDH* at 72hpi. Three biological replicates shown. For a, c–f mean \pm SEM or independent datapoints are shown. For b, box and whisker blots show 10–90 percentile and groups were compared at each time point as indicated using a Kruskal-Wallis test. For c, groups were compared by an unpaired two-tailed Student's t-Test. For d and f, one-way ANOVA with a Bonferroni post-test was used. For e, two-way ANOVA and Bonferroni post-test was used.



Extended Data Fig. 6 | Innate immune phenotype of dominant Omicron subvariants. (a) Absolute global SARS-CoV-2 variant sequence counts over time, extracted from CoV-Spectrum using genomic data from GISAID. (b) ACE2/TMPRSS2-A549 cells were infected with 2000 Nsp12 copies/cell of the indicated SARS-CoV-2 variants in the presence of DMSO, 25 μ M E64d or 25 μ M Camostat. Infection levels were determined by N-positivity at 24hpi. (c-e) SARS-CoV-2 Omicron subvariants infection of Calu-3 cells determined by N-positivity over time for the indicated subvariants in cells from Fig. 4b-d with (c) BA.2.75 (yellow; O), (d) XBB-subvariants (XBB.1: light red, O; XBB.1(B): red, Δ ; XBB.1.5: dark red, \square) and (e) BQ.1.1 (BQ.1.1: light green, O; BQ.1.1(B): dark green, Δ) isolates shown. (f-h) HAEs were infected with 1500 E copies/cell of the indicated variants. Viral replication was measured by viral release into apical washes over time in cells

from Fig. 4e. (f) BA.2.75, (g) XBB-subvariants and (h) BQ.1.1 isolates are shown compared to BA.2 (blue) and BA.5 (purple). (i) Infection levels of indicated variants in Calu-3 cells in the presence or absence of 5 μ M ruxolitinib at 48hpi in cells from Fig. 4g. (j-l) Quantification of two independent western blots showing (j) STAT1-pY701, (k) total IRF3 and (l) total STAT1 over β -actin at 24hpi. For b, treatments were compared to DMSO for each variant using one-way ANOVA and Dunnett's post-test. For c-i, variant infection levels were compared to BA.2 at each time point by two-way ANOVA and Bonferroni post-test. Colors indicate comparator (BA.5, purple; BA.2.75, yellow; XBB.1, light red; XBB.1(B), red; XBB.1.5, dark red; BQ.1.1, light green; BQ.1.1(B), dark green). Replicate measurements from one of three independent experiments. Fold change over mock is shown. Mean \pm SEM or individual datapoints are shown. hpi, hours post infection.



Extended Data Fig. 7 | Gating strategy for flow cytometry analysis of nucleocapsid expression. Representative gating strategy shown. Nucleocapsid-positive cells (N+) were identified by intracellular staining for SARS-CoV-2 N. Positive gates were determined based on uninfected (mock) cells.

Extended Data Table 1 | Orf6 mutations detected in the Omicron subvariants

| | BA.1 | BA.2 | BA.4 | BA.5 |
|---|------|------|------|------|
| A27259C (synonymous) | + | + | + | – |
| G27382C, A27383T, T27384C (non-synonymous: D61L) | – | + | + | – |

Presence of Orf6 mutations in BA.1, BA.2, BA.4 and BA.5 at the indicated positions compared to the reference sequence hCoV-19/Wuhan/WIV04/2019 (WIV04) (EPI_ISL_402124). Nucleotide and (non-synonymous amino acid) changes indicated. No mutations were detected in the region of the M gene surrounding the Orf6 TRS at position 27041-27046 (core TRS ACGAAC).

Extended Data Table 2 | Nucleocapsid (N) mutations detected in the Omicron subvariants

| | BA.1 | BA.2 | BA.4 | BA.5 |
|--|-------------|-------------|-------------|-------------|
| C28311T (non-synonymous: P13L) | + | + | + | + |
| A28330G (synonymous) | – | – | – | + |
| A28363T (synonymous) | + | + | + | + |
| Deletion 28364-28372 (31-33del) | + | + | + | + |
| C28724T (non-synonymous: P151S) | – | – | + | – |
| G28881A, G28882A (non-synonymous R203K [†]) | + | + | + | + |
| G28883C (non-synonymous G204R [†]) | + | + | + | + |
| A29510C (non-synonymous S413R) | – | + | + | + |

Presence of N mutations in BA.1, BA.2, BA.4 and BA.5 at the indicated positions compared to the reference sequence hCoV-19/Wuhan/WIV04/2019 (WIV04) (EPI_ISL_402124). Nucleotide and (non-synonymous amino acid) changes indicated. BA. 1, BA.2, BA.4 and BA.5 carry nucleotide substitution A28271T, changing their Kozak initiation context from adequate (A in –3, T in +4) to the weak (T in –3, T in +4) as previously described¹⁶.

[†]The non-synonymous mutations R203K-G204R confer a partial TRS for N* sgRNA¹⁶.

Reporting Summary

Nature Portfolio wishes to improve the reproducibility of the work that we publish. This form provides structure for consistency and transparency in reporting. For further information on Nature Portfolio policies, see our [Editorial Policies](#) and the [Editorial Policy Checklist](#).

Statistics

For all statistical analyses, confirm that the following items are present in the figure legend, table legend, main text, or Methods section.

- | n/a | Confirmed |
|-------------------------------------|--|
| <input type="checkbox"/> | <input checked="" type="checkbox"/> The exact sample size (n) for each experimental group/condition, given as a discrete number and unit of measurement |
| <input type="checkbox"/> | <input checked="" type="checkbox"/> A statement on whether measurements were taken from distinct samples or whether the same sample was measured repeatedly |
| <input type="checkbox"/> | <input checked="" type="checkbox"/> The statistical test(s) used AND whether they are one- or two-sided <i>Only common tests should be described solely by name; describe more complex techniques in the Methods section.</i> |
| <input type="checkbox"/> | <input checked="" type="checkbox"/> A description of all covariates tested |
| <input type="checkbox"/> | <input checked="" type="checkbox"/> A description of any assumptions or corrections, such as tests of normality and adjustment for multiple comparisons |
| <input type="checkbox"/> | <input checked="" type="checkbox"/> A full description of the statistical parameters including central tendency (e.g. means) or other basic estimates (e.g. regression coefficient) AND variation (e.g. standard deviation) or associated estimates of uncertainty (e.g. confidence intervals) |
| <input type="checkbox"/> | <input checked="" type="checkbox"/> For null hypothesis testing, the test statistic (e.g. F , t , r) with confidence intervals, effect sizes, degrees of freedom and P value noted <i>Give P values as exact values whenever suitable.</i> |
| <input checked="" type="checkbox"/> | <input type="checkbox"/> For Bayesian analysis, information on the choice of priors and Markov chain Monte Carlo settings |
| <input checked="" type="checkbox"/> | <input type="checkbox"/> For hierarchical and complex designs, identification of the appropriate level for tests and full reporting of outcomes |
| <input checked="" type="checkbox"/> | <input type="checkbox"/> Estimates of effect sizes (e.g. Cohen's d , Pearson's r), indicating how they were calculated |

Our web collection on [statistics for biologists](#) contains articles on many of the points above.

Software and code

Policy information about [availability of computer code](#)

Data collection: BD FACSDiva Software Verison 9.0 (BD), Odyssey Infrared Imager software Image Studia Lite V5.2, 7500 Software (Applied Biosystems), WiScan® Hermes 7-Colour High-Content Imaging System (IDEA Bio-Medical).

Data analysis: FlowJo v10.6.2 (Tree Star); Design & Analysis Software Version: 2.6.2 (Thermo Fisher Scientific); Image Studia Lite V5.2 (LI-COR); GraphPad Prism9 Versino 9.0.0; FIJI ImageJ software package40; Athena Image analysis software (IDEA Bio-Medical)

For manuscripts utilizing custom algorithms or software that are central to the research but not yet described in published literature, software must be made available to editors and reviewers. We strongly encourage code deposition in a community repository (e.g. GitHub). See the Nature Portfolio [guidelines for submitting code & software](#) for further information.

Data

Policy information about [availability of data](#)

All manuscripts must include a [data availability statement](#). This statement should provide the following information, where applicable:

- Accession codes, unique identifiers, or web links for publicly available datasets
- A description of any restrictions on data availability
- For clinical datasets or third party data, please ensure that the statement adheres to our [policy](#)

All data generated or analysed during this study are included in this manuscript (and its supplementary information files). SARS-CoV-2 sequence counts were extracted from CoV-Spectrum (cov-spectrum.org) using genomic data from GSAID. No new algorithms were developed for this project.

Human research participants

Policy information about [studies involving human research participants and Sex and Gender in Research](#).

| | |
|-----------------------------|--|
| Reporting on sex and gender | <input type="text" value="Not applicable."/> |
| Population characteristics | <input type="text" value="Not applicable."/> |
| Recruitment | <input type="text" value="Not applicable."/> |
| Ethics oversight | <input type="text" value="Not applicable."/> |

Note that full information on the approval of the study protocol must also be provided in the manuscript.

Field-specific reporting

Please select the one below that is the best fit for your research. If you are not sure, read the appropriate sections before making your selection.

Life sciences Behavioural & social sciences Ecological, evolutionary & environmental sciences

For a reference copy of the document with all sections, see [nature.com/documents/nr-reporting-summary-flat.pdf](https://www.nature.com/documents/nr-reporting-summary-flat.pdf)

Life sciences study design

All studies must disclose on these points even when the disclosure is negative.

| | |
|-----------------|---|
| Sample size | <input type="text" value="No statistical methods were used to pre-determine sample sizes but our sample sizes are similar to those reported in previous publications (Thorne et al, 2022, Nature; Thorne et al, 2021, EMBO J). Multiple independent experiments were repeated to allow for appropriate statistical analysis."/> |
| Data exclusions | <input type="text" value="No data were excluded."/> |
| Replication | <input type="text" value="In vitro experiments were performed independently a minimum of 3 times (unless otherwise stated) to allow for appropriate confidence. All attempts at replication were successful."/> |
| Randomization | <input type="text" value="No randomisation was performed. Experimental groups were treated identical except for the specific variable being tested, thus randomisation is not required."/> |
| Blinding | <input type="text" value="Blinding was not necessary all measurements were quantified by automated machines, and no data were excluded."/> |

Reporting for specific materials, systems and methods

We require information from authors about some types of materials, experimental systems and methods used in many studies. Here, indicate whether each material, system or method listed is relevant to your study. If you are not sure if a list item applies to your research, read the appropriate section before selecting a response.

| Materials & experimental systems | | Methods | |
|-------------------------------------|---|-------------------------------------|--|
| n/a | Involvement in the study | n/a | Involvement in the study |
| <input type="checkbox"/> | <input checked="" type="checkbox"/> Antibodies | <input checked="" type="checkbox"/> | <input type="checkbox"/> ChIP-seq |
| <input type="checkbox"/> | <input checked="" type="checkbox"/> Eukaryotic cell lines | <input type="checkbox"/> | <input checked="" type="checkbox"/> Flow cytometry |
| <input checked="" type="checkbox"/> | <input type="checkbox"/> Palaeontology and archaeology | <input checked="" type="checkbox"/> | <input type="checkbox"/> MRI-based neuroimaging |
| <input checked="" type="checkbox"/> | <input type="checkbox"/> Animals and other organisms | | |
| <input checked="" type="checkbox"/> | <input type="checkbox"/> Clinical data | | |
| <input checked="" type="checkbox"/> | <input type="checkbox"/> Dual use research of concern | | |

Antibodies

| | |
|-----------------|--|
| Antibodies used | <input type="text" value="For flowcytometry and western blot: CR3009 SARS-CoV-2 cross-reactive antibody (a gift from Laura McCoy); secondary Alexa Fluor 488-Donkey-anti-Human IgG (Jackson Labs); rabbit-anti-SARS spike (Invitrogen, PA1-411-1165), mouse-anti-SARS-CoV-2 spike (GeneTex 1A9), rabbit-anti-Orf6 (Abnova, PAB31757), rabbit-anti-Orf9b (ProSci, 9191), rabbit-anti-phospho-STAT1 (Ser727) (CellSignaling, Cat # 9177), rabbit-anti-phospho"/> |
|-----------------|--|

STAT1 (Tyr 701) (CellSignaling, Cat# 9167, clone 58D6), rabbit-anti-STAT1 (CellSignaling, Cat# 9172), anit-rabbit-IRF3 (CellSignaling, Cat# 4302), rabbit-anti-phospho IRF3 (CellSignaling, Cat# 29047, clone D6O1M) and rabbit-anti-beta-actin (A2066, SIGMA), IRDye 800CW or 680RD secondary antibodies (Abcam, goat anti-rabbit, goat anti-mouse or goat anti-human).

For immunofluorescence microscopy:

Rabbit-anti-IRF3 antibody (sc-33641, Santa Cruz), rabbit-anti-STAT-1 (D1K9Y, Abcam), mouse-anti-dsRNA (MABE1134, Millipore) and Cr3009 SARS-CoV cross-reactive human-anti-N antibodies; anti-rabbit-AlexaFluor-488, anti-mouse-AlexaFluor-568 and anti-human-Alexa647 conjugates (Jackson ImmunoResearch).

Validation

Validation for commercial antibodies and target specificity was confirmed in the technical data sheets provided by the manufacturer, containing example data and relevant citations. Furthermore, negative controls (uninfected cells) were included in experiments to confirm absence of or low non-specific binding of antibodies.

CR3009 SARS-CoV-2 cross-reactive: described and validated here <https://www.nibsc.org/documents/ifu/101009.pdf>
rabbit-anti-SARS spike (Invitrogen, PA1-411-1165), validated by the manufacturer: <https://www.thermofisher.com/antibody/product/SARS-Coronavirus-Spike-Protein-Antibody-Polyclonal/PA1-41165>

mouse-anti-SARS-CoV-2 spike (GeneTex 1A9), validated by the manufacturer. This antibody detects both SARS-CoV spike and SARS-CoV-2 spike proteins (S2 subunit). Based on sequence analysis, this antibody is predicted to recognize S2' subunit. Our internal testing indicates no cross-reactivity with MERS-CoV spike protein. This antibody is able to detect multiple SARS-CoV-2 VOCs, including Omicron variant. <https://www.genetex.com/Product/Detail/SARS-CoV-SARS-CoV-2-COVID-19-spike-antibody-1A9/GTX632604>
rabbit-anti-Orf6 (Abnova, PAB31757), details in the technical datasheet: https://www.abnova.com/upload/media/product/document/2020/DS_PAB31757.pdf

rabbit-anti-Orf9b (ProSci, 9191), details provided by the manufacturer: <https://www.prosci-inc.com/product/sars-cov-2-covid-19-orf9b-antibody-9191/>

rabbit-anti-phospho-STAT1 (Ser727) (CellSignaling, Cat # 9177), Phospho-Stat1 (Ser727) Antibody detects endogenous levels of Stat1 α only when phosphorylated at Ser727. This site is deleted in Stat1 β . This antibody does not significantly cross-react with the corresponding phosphorylated residues of other Stat proteins. <https://www.cellsignal.com/products/primary-antibodies/phospho-stat1-ser727-antibody/9177>

rabbit-anti-phospho STAT1 (Tyr 701) (CellSignaling, Cat# 9167, clone 58D6), Phospho-Stat1 (Tyr701) (58D6) Rabbit mAb detects endogenous levels of Stat1 only when phosphorylated at tyrosine 701. The antibody detects phosphorylated tyrosine 701 of p91 Stat1 and also the p84 splice variant. It does not cross-react with the corresponding phospho-tyrosines of other Stat proteins. <https://www.cellsignal.com/products/primary-antibodies/phospho-stat1-tyr701-58d6-rabbit-mab/9167>

rabbit-anti-STAT1 (CellSignaling, Cat# 9172), Stat1 Antibody detects endogenous levels of total Stat1 protein. The antibody detects both Stat1 α (91kDa) and Stat1 β (84 kDa) isoforms. <https://www.cellsignal.com/products/primary-antibodies/stat1-antibody/9172>

anit-rabbit-IRF3 (CellSignaling, Cat# 4302), IRF-3 (D83B9) Rabbit mAb detects endogenous levels of total IRF-3 protein. <https://www.cellsignal.com/products/primary-antibodies/irf-3-d83b9-rabbit-mab/4302>

rabbit-anti-phospho IRF3 (CellSignaling, Cat# 29047, clone D6O1M); Phospho-IRF-3 (Ser396) (D6O1M) Rabbit mAb recognizes endogenous levels of IRF-3 protein only when phosphorylated at Ser396. <https://www.cellsignal.com/products/primary-antibodies/phospho-irf-3-ser396-d6o1m-rabbit-mab/29047>

rabbit-anti-beta-actin (A2066, SIGMA), validation and details provided by the manufacturer: <https://www.sigmaaldrich.com/GB/en/product/sigma/a2066>

Rabbit-anti-IRF3 antibody (sc-33641, Santa Cruz), IRF-3 (SL-12) is recommended for detection of IRF-3 of mouse, rat and human origin. <https://datasheets.scbt.com/sc-33641.pdf>

rabbit-anti-STAT-1 (CellSignaling, Cat# 14994, clone D1K9Y), Stat1 (D1K9Y) Rabbit mAb recognizes endogenous levels of total Stat1 protein. This antibody also cross-reacts with an unidentified protein of 150 kDa. <https://www.cellsignal.com/products/primary-antibodies/stat1-d1k9y-rabbit-mab/14994>

mouse-anti-dsRNA (MABE1134, Millipore), Clone rJ2 specifically recognizes double stranded RNA (dsRNA) of greater than 40 bp in length that is generated during the replication of positive sense genome viruses. https://www.merckmillipore.com/GB/en/product/Anti-dsRNA-Antibody-clone-rJ2,MM_NF-MABE1134-25UL

Eukaryotic cell lines

Policy information about [cell lines and Sex and Gender in Research](#)

Cell line source(s)

Calu-3 cells were purchased from AddexBio (C0016001), Caco-2 cells were a kind gift from Dalan Bailey (Pirbright Institute) and HeLa-ACE2 cells were a gift from James E Voss described in Rogers et al, 2020, Science. A459 cells expressing ACE2 and TMPRSS2 were a gift from Massimo Palmarini (CVR, Glasgow) described in Willet et al., 2022, Nature Microbiology.

Authentication

Cell lines were commercially procured and confirmed to be the cell lines indicated and mycoplasma-free by the supplier. Cell lines that were received from collaborators were confirmed to be the cell lines indicated by the respective labs.

Mycoplasma contamination

Random mycoplasma testing was conducted and cells tested negative.

Commonly misidentified lines (See [ICLAC](#) register)

None

Flow Cytometry

Plots

Confirm that:

- The axis labels state the marker and fluorochrome used (e.g. CD4-FITC).
- The axis scales are clearly visible. Include numbers along axes only for bottom left plot of group (a 'group' is an analysis of identical markers).
- All plots are contour plots with outliers or pseudocolor plots.
- A numerical value for number of cells or percentage (with statistics) is provided.

Methodology

Sample preparation

Adherent cells were trypsinised and fixed in 4% formaldehyde prior to intracellular staining for SARS-CoV-2 nucleocapsid (N) protein. For N detection, cells were permeabilised for 15 min with Intracellular Staining Perm Wash Buffer (BioLegend) and subsequently incubated with 1µg/ml CR3009 SARS-CoV-2 cross-reactive antibody (a gift from Laura McCoy) for 30 min at room temperature. Primary antibodies were detected by incubation with secondary Alexa Fluor 488-Donkey-anti-Human IgG (Jackson Labs).

Instrument

All samples were acquired on a BD Fortessa X20 or LSR II using BD FACSDiva software.

Software

Data was analysed using FlowJo v10 (Tree Star).

Cell population abundance

N/A. Flowcytometry was used to determine SARS-CoV-2 infection levels in Calu-3 monocultures.

Gating strategy

Infected cells were identified as follows: Calu-3 cells identified by SSC-A vs FSC-A -> Singlets (FSC-A vs FSC-H) -> Nucleocapsid positive cells (N+) (gated on uninfected cells)

- Tick this box to confirm that a figure exemplifying the gating strategy is provided in the Supplementary Information.